The Astrophysical Journal, 909:121 (26pp), 2021 March 10 https://doi.org/10.3847/1538-4357/abe0b5

Looking for Obscured Young Star Clusters in NGC 1313

Matteo Messa[1], Daniela Calzetti[1], Angela Adamo[2], Kathryn Grasha[3,4], Kelsey E. Johnson[5], Elena Sabbi[6], Linda J. Smith[7], Varun Bajaj[6], Molly K. Finn[5], and Zesen Lin[8]
[1] Department of Astronomy, University of Massachusetts Amherst, 710 North Pleasant Street, Amherst, MA 01003, USA; matteo.messa@unige.ch
[2] Department of Astronomy, Oscar Klein Centre, Stockholm University, AlbaNova, Stockholm SE-106 91, Sweden
[3] Research School of Astronomy and Astrophysics, Australian National University, Weston Creek, ACT 2611, Australia
[4] ARC Centre of Excellence for All Sky Astrophysics in 3 Dimensions (ASTRO 3D), Australia
[5] Department of Astronomy, University of Virginia, Charlottesville, VA 22904-4325, USA
[6] Space Telescope Science Institute, 3700 San Martin Drive, Baltimore, MD 2121, USA
[7] Space Telescope Science Institute and European Space Agency, 3700 San Martin Drive, Baltimore, MD 21218, USA
[8] Key Laboratory for Research in Galaxies and Cosmology, Department of Astronomy, University of Science and Technology of China, Hefei 230026, People's Republic of China
Received 2020 November 18; revised 2021 January 25; accepted 2021 January 26; published 2021 March 11

Abstract

Using recently acquired Hubble Space Telescope NIR observations (J, Paβ, and H bands) of the nearby galaxy NGC 1313, we investigate the timescales required by a young star cluster to emerge from its natal cloud. We search for extincted star clusters, potentially embedded in their natal cloud as either (1) compact sources in regions with high Hα/Paβ extinctions or (2) compact H II regions that appear as point-like sources in the Paβ emission map. The NUV–optical–NIR photometry of the candidate clusters is used to derive their ages, masses, and extinctions via a least-χ^2 spectral energy distribution broad- and narrowband fitting process. The 100 clusters in the final samples have masses in the range $\log_{10}(M/M_{\odot}) = 2.5$–$3.5$ and moderate extinctions, $E(B-V) \lesssim 1.0$ mag. Focusing on the young clusters (0–6 Myr), we derive a weak correlation between extinction and age of the clusters. Almost half of the clusters have low extinctions, $E(B-V) < 0.25$ mag, already at very young ages ($\leqslant$3 Myr), suggesting that dust is quickly removed from clusters. A stronger correlation is found between the morphology of the nebular emission (compact, partial or absent, both in Hα and Paβ) and cluster age. Relative fractions of clusters associated with a specific nebular morphology are used to estimate the typical timescales for clearing the natal gas cloud, resulting in between 3 and 5 Myr, ∼1 Myr older than what was estimated from NUV–optical-based cluster studies. This difference hints at a bias for optical-only-based studies, which James Webb Space Telescope will address in the coming years.

Unified Astronomy Thesaurus concepts: Young star clusters (1833); Compact H II region (286); Star formation (1569); Interstellar dust extinction (837); Spiral galaxies (1560)

Supporting material: machine-readable table

1. Introduction

Recent studies comparing the spatial distribution within galaxies of giant molecular clouds (GMCs) and H II regions suggest that GMCs spend most of their lifetime in an inert state. From the moment they begin to host star formation, their dense cores are quickly dissolved, on timescales of a few million years (Kobulnicky & Johnson 1999; Matthews et al. 2018; Kruijssen et al. 2019). Such short timescales, suggesting very efficient feedback from young stars, have been found with the same technique in various nearby galaxies and at different galactocentric distances (Kruijssen et al. 2019; Chevance et al. 2020a). According to these results, the star formation process is rapid and inefficient because feedback acts on very short timescales, resulting in only a small fraction of the gas being converted into stars (e.g., Matthews et al. 2018; Chevance et al. 2020b).

Short feedback timescales have been typically derived in recent years by comparing tracers of different stages of the star formation (SF) process. Corbelli et al. (2017) studied GMCs, embedded clusters (in the mid-infrared, MIR, where the extinction effect is lower), and exposed clusters (in Hα and UV bands) in the nearby galaxy M33, finding that young clusters remain in an embedded phase only for ∼2 Myr on average. Similarly, Grasha et al. (2018, 2019) found median ages of 2–4 Myr for clusters associated with GMCs in NGC 7793 and NGC 5194, while Whitmore et al. (2014) found clearing timescales of ∼5 Myr for young clusters. This also suggests that star clusters are able to emerge from their natal clouds long before the timescale required for clouds to disperse.

Star clusters play a fundamental role in the SF process, as most of the SF takes place in clustered environments (Lada & Lada 2003), and typically ∼5%–20% of the stars formed will evolve into bound systems (e.g., Bastian et al. 2012; Adamo et al. 2015; Chandar et al. 2015; Johnson et al. 2016; Messa et al. 2018a, 2018b and the review by Krumholz et al. 2019). Clustered star formation hosts most of the massive stars, responsible for the feedback regulating SF processes. The very early stages of cluster evolution can thus reveal, via the time needed to clear the gas and dust cloud around them, which feedback mechanism is mostly responsible for stopping star formation and therefore determining its efficiency. Whitmore et al. (2011) and Hollyhead et al. (2015) studied the morphologies of Hα emission associated with young clusters in the nearby galaxy M83, revealing that clusters are no longer embedded in their natal gas clouds by ages <4 Myr, in agreement with the aforementioned studies of GMCs–clusters association. Hannon et al. (2019) measured a progression of the median ages when going from concentrated H II regions (median age ∼3 Myr) to partially exposed (∼4 Myr) to no Hα emission (>5 Myr). The same authors suggest that the typical timescale for gas clearing can be very short, on the order of ∼2 Myr.

Almost all extragalactic young cluster studies are based on NUV–optical bands and therefore could be biased against

extincted clusters (with extinctions higher than $A_V \gtrsim 1.0$ mag). Embedded clusters are likely extincted in the optical bands and can be revealed with longer wavelength emission. Radio observations can be used to directly detect the free–free emission from the gas ionized by newly formed massive stars (e.g., Kobulnicky & Johnson 1999; Johnson et al. 2001, 2004, 2009; Johnson & Kobulnicky 2003; Turner & Beck 2004; Aversa et al. 2011; Kepley et al. 2014). The low detection rate of compact thermal radio sources is consistent with this embedded phase being short lived (e.g., Tsai et al. 2009; Aversa et al. 2011). Millimeter (and submillimeter) observations enable us to probe the molecular material in the vicinity of young star clusters (e.g., Johnson et al. 2015, 2018; Finn et al. 2019). Infrared emission can be used to trace the warm dust cocoons surrounding young clusters (e.g., Vacca et al. 2002; Johnson et al. 2004; Corbelli et al. 2017), although the extent to which the infrared luminosities and colors can be used as diagnostics is highly dependent on the physical distribution of dust (e.g., Whelan et al. 2011). Fully constraining the characteristics of embedded clusters requires this full wavelength coverage (from the radio to the infrared).

Typical mid-infrared (MIR) resolution (point-spread function (PSF) − FWHM $\gtrsim 1\farcs9$ for Spitzer) allows us to resolve single clusters only for galaxies at close distances $\lesssim$1 Mpc, making it difficult to build statistical samples. Already at a few Mpc, the SF clumps observable in the MIR bands may contain several star clusters (see, e.g., Lin et al. 2020). Studying MIR clumps on such scales (∼50 pc) reveal sources with foreground extinctions up to $A_V \sim 15$ mag (Elmegreen & Elmegreen 2019) and are useful to study the collapse of gas clouds (Elmegreen et al. 2018; Elmegreen & Elmegreen 2019, 2020) but cannot trace the effect of feedback on the ∼parsec scale. The main unknown of the current studies on gas-clearing timescales is the possible effect of young embedded (and therefore possibly extincted) clusters, which are consistently ignored in studies of cluster populations focused on the optical–NUV bands (e.g., Whitmore et al. 2011; Hollyhead et al. 2015; Hannon et al. 2019). With the present work, we are filling this gap by targeting the young and embedded clusters.

One way of combining high spatial resolution with the study of embedded star clusters is to rely on the infrared bands of the Hubble Space Telescope (HST). It is expected that newly formed clusters are surrounded by a dense compact (with radii of ∼1 pc) cloud of gas and dust, which makes them extincted in the optical and NUV bands. Calzetti et al. (2015a) already demonstrated how the use of the near-infrared (NIR) HST band, and in particular the presence of NIR narrowband filters, helps to characterize a highly extincted cluster (with foreground extinction $A_V \sim 2$ mag and mixed attenuation from a cloud of $A_V \sim 49$ mag in total), detected in the optical spectrum only in the *I* band, in the center of NGC 5253.

In this work, we extend the NIR study of embedded clusters in the nearby galaxy NGC 1313, a mildly inclined ($i = 40\fdg7$) SBd galaxy at a distance of 4.39 ± 0.04 Mpc (Jacobs et al. 2009). Similarly to the study of Calzetti et al. (2015a), we will use newly acquired HST-WFC3 NIR data, namely F110W, F128N, and F160W, corresponding to the *J*, Paβ, and *H* bands. NGC 1313 has a stellar mass of $2.6 \times 10^9\,M_\odot$, an extinction-corrected $\mathrm{SFR_{UV}} = 1.15\,M_\odot\,\mathrm{yr}^{-1}$ (Calzetti et al. 2015b), and has been suggested to be currently in interaction with a satellite galaxy that has produced a loop of H I gas around the galaxy (Peters et al. 1994) and a recent increase (on a timescale of 100 Myr) of the SFR in the southwest arm (Silva-Villa & Larsen 2012). Due to both its physical and morphological properties, with the presence of a bar and a rather irregular appearance, NGC 1313 has been compared to the Large Magellanic Cloud (de Vaucouleurs 1963). The star cluster population of NGC 1313 is quite numerous, with 673 clusters with ages <300 Myr (Grasha et al. 2017b), of which 195 have compact morphology, ages ⩽200 Myr, and masses $\geqslant 5000\,M_\odot$ (Ryon et al. 2017). The proximity of the galaxy, combined with the HST resolution, allowed its cluster population on physical scales $\lesssim$1 pc to be studied, and Ryon et al. (2017) find a median cluster size of 2.3 pc. Using HST narrowband observations of NGC 1313 and of two galaxies at a similar distance, Hannon et al. (2019) studied the morphology of Hα regions associated with the star clusters, estimating the typical timescales for a compact gas nebula to disperse (<5 Myr). We will, in the current work, complement the Hannon et al. (2019) study with our new NIR-based analysis.

The paper is organized as follows: in Section 2 we present the HST observations used in this study, while in Section 3 we describe the methodology used to extract the catalogs of the young cluster candidates. In Sections 4 and 5 we present the analysis performed and the relative results. We discuss the results of our analysis in Section 6 and summarize our findings in Section 7.

2. Data

Recently acquired near-infrared (NIR) photometry of NGC 1313 with the WFC3-IR camera, on board HST, covers two pointings of the galaxy with two broadband (F110W and F160W) and one narrowband (F128N) filters (GO program 15330; PI D. Calzetti). The narrowband filter, centered at 1.283 μm, covers the wavelengths of the Paschen-β (Paβ) hydrogen recombination line emission. For each filter, individual exposures were corrected for bias, dark, and flat-field using the standard pipeline CALWF3 version 3.4.2. Images were aligned to the Gaia DR2 (Gaia Collaboration et al. 2018) reference frame using TweakReg and mosaicked together using AstroDrizzle to a pixel scale of 0.08 arcsec pixel^{-1}. Proper motions were not applied in the alignment, as the high uncertainties of proper motions of extragalactic sources in the DR2 catalog would yield worse alignments and poor subsampling in the mosaics. In this study, we take advantage of the broad archival HST wavelength coverage of NGC 1313; in detail, we use observations in five filters from the Legacy ExtraGalactic UV Survey (LEGUS; Calzetti et al. 2015b) covering the NUV–optical range with broadband filters (F275W, F336W, F435W, F555W, and F814W) and in two additional filters from the LEGUS-Hα follow-up survey (GO 13773; PI R. Chandar) observing the galaxy with a narrow filter covering the Hα emission-line (F657N) and a medium-band filter sampling the line-free continuum (F547M). In total, we have 10 filters spanning the wavelength range NUV–NIR, including two filters for the observation of the two hydrogen recombination lines Hα and Paβ; details of the observations are summarized in Table 1. Figure 1 (top left) shows an RGB composite with Hα, F555W, and Paβ in the blue, green, and red channels, respectively. We study the cluster population in the area delimited by the field of view of the NIR pointings, outlined in the same figure.

3. Source Catalogs

We look for young dust-embedded star clusters following two separate approaches: (1) we define regions of high extinction by constructing an extinction map from the combination of Hα and Paβ emission-line maps and looking for NIR compact sources within such regions; and (2) we select, within the entire galaxy,

Table 1
Summary of the HST Observations Used in this Work, along with the Pivot Wavelength of Each Filter (P_λ) and the Exposure Times (Expt)

Instrument	Filter	P_λ (Å)	Expt (s)	Np	Program/PI	Date
WFC3-IR	F160W	15369	3594	2	GO 15330/Calzetti	2017-11-26, 2018-09-04
WFC3-IR	F128W	12832	5994	2	GO 15330/Calzetti	2017-11-26, 2018-09-04
WFC3-IR	F110W	11534	1994	2	GO 15330/Calzetti	2017-11-26, 2018-09-04
ACS-WFC	F814W	8047	4569	5	GO 9796/Miller	2003-11-17
					GO 9774/Larsen	2004-05-27, 2004-07-17, 2004-12-18
					GO 10210/Tully	2004-10-30
WFC3-UVIS	F657N	6567	3090	2	GO 13773/Chandar	2015-02-24, 2016-02-14
WFC3-UVIS	F547M	5447	1108	2	GO 13773/Chandar	2015-02-24, 2016-02-14
ACS-WFC	F555W	5360	5600	5	GO 9796/Miller	2003-11-17, 2004-02-22
					GO 9774/Larsen	2004-05-27, 2004-07-17, 2004-12-18
ACS-WFC	F435W	4329	4560	4	GO 9796/Miller	2003-11-17
					GO 9774/Larsen	2004-05-27, 2004-07-17, 2004-12-18
WFC3-UVIS	F336W	3355	4818	2	GO 13364/Calzetti	2014-02-16, 2014-02-19
WFC3-UVIS	F275W	2707	5058	2	GO 13364/Calzetti	2014-02-16, 2014-02-19

Note. The exposure times refer to the total time summing up all the pointings (Np) in each filter. For F814W, F555W, and F435W, data from multiple programs are used.

sources with compact Paβ line emission. In addition to the aforementioned source selections, we also consider the cluster catalog produced by LEGUS Adamo et al. (2017), based on HST observation in five NUV–optical broadband filters.

3.1. Sources in High-extinction Regions

We make use of the observations in the UVIS-F657N and IR-F128N filters to construct Hα and Paβ nebular emission-line maps. In order to estimate the continuum emission at the central wavelength of the F657N filter, we use two nearby filters, F547M and F814W. The former is a medium-band filter not containing nebular lines, the latter, however, does contain emission lines, but its large bandwidth causes the flux to be greatly dominated, even for very young sources, by the stellar continuum; the nebular lines play only a minimal contribution. We linearly interpolate the observed flux on a logarithmic scale in those two filters on a pixel-by-pixel basis, and we find, for every pixel of the data, the continuum corresponding to the pivot wavelength of the F657N filter, $\lambda_{\rm F657N} = 6566.6$ Å. This approach is made possible by the comparable widths of the PSF in the various HST optical filters, ensuring that the contribution to the flux in every pixel comes from the same region in every observed band. Having subtracted the continuum, we are left with the combined emission of the Hα line and the [N II] doublet ($\lambda\lambda$6548, 6584 Å). In order to remove the contribution of the [N II] lines from the emission, we use their relative ratio to the Hα line as given by Kennicutt et al. (2008; for NGC 1313, [N II]/H$\alpha = 0.34$).

We create a map of the Paβ emission in a similar way, using F110W and F160W as nearby filters. We interpolate the flux in those two filters to estimate the value of the stellar continuum at the pivot wavelength of the F128N filter, $\lambda_{\rm F128N} = 12831.8$ Å. We point out that the F110W filter contains the Paβ emission and, therefore, we use the first estimate of the Paβ line emission map to create a line-free F110W map and then repeat the interpolation process. The second estimate of the Paβ emission-line map differs from the first one by 5% at maximum. Further iterations of this "cleaning" process differ from the previous ones by less than 0.1% and quickly converge.

We convert the Hα and Paβ emission maps to a common physical resolution by degrading the pixel scale of the Hα map from 0.04 to 0.08 arcsec pix^{-1} and then convolve each map to a Gaussian kernel with $\sigma = 3$ px ($\sim$5 pc at the distance of NGC 1313), in order to smooth possible pixel-scale inaccuracies of the maps. We calculate the ratio Hα/Paβ, correcting for the Galactic reddening:

$$R_{\rm dered.} \equiv \left(\frac{\rm H\alpha}{\rm Pa\beta}\right)_{\rm dered.} = \left(\frac{\rm H\alpha}{\rm Pa\beta}\right)_{\rm observed} 10^{0.4\cdot[k({\rm H\alpha})-k({\rm P\beta})]\cdot E(B-V)}, \quad (1)$$

where, for the Milky Way extinction law, $k({\rm H\alpha}) - k({\rm P\beta}) = 1.69$ (according to the parameterization of Fitzpatrick 1999, with total-to-selective extinction value $R_V = 3.1$), and we used $E(B-V) = 0.096$ mag[9] for the foreground extinction correction in the direction of NGC 1313. Finally, we convert the line ratio into an expected extinction value. Taking the intrinsic line ratio $R_{\rm intrinsic} = 17.57$,[10] we assume that the different ratios observed over the different subregions of the galaxies are due to variations in the nebular extinction:

$$A_V = \frac{R_V}{-0.4\cdot[k({\rm H\alpha}) - k({\rm P\beta})]} \cdot \log_{10}\left(\frac{R_{\rm dered.}}{R_{\rm intrinsic}}\right), \quad (2)$$

with $R_V = 3.1$. In constructing the extinction map, we limit our selection to regions where both Hα and Paβ line emissions have a signal-to-noise ratio (S/N) > 3.

We show the extinction map in Figure 1. In the same figure, as well as in Figure 2, we compare it to the 8 μm emission from the Spitzer telescope, revealing the dust emission. We find good spatial coincidence of the extincted nebular regions with the regions of brightest emission in 8 μm. As expected, the extinction map reveals the extended regions along the spiral arms of NGC 1313 associated with recent star formation. In more details, the extinction and the 8 μm maps highlight three main extended extincted regions, two on the eastern side of the galaxy and one on the western side. In addition, the extinction map reveals compact regions with elevated A_V values, associated with single sources; these latter cases are frequently caused by sources with high Paβ emission but almost no Hα, mostly located along the spiral arms but with some exceptions.

[9] Value taken from the NASA Extragalactic Database (NED).
[10] Appropriate for H II regions with electron temperature $T_e \sim 11{,}500$ K.

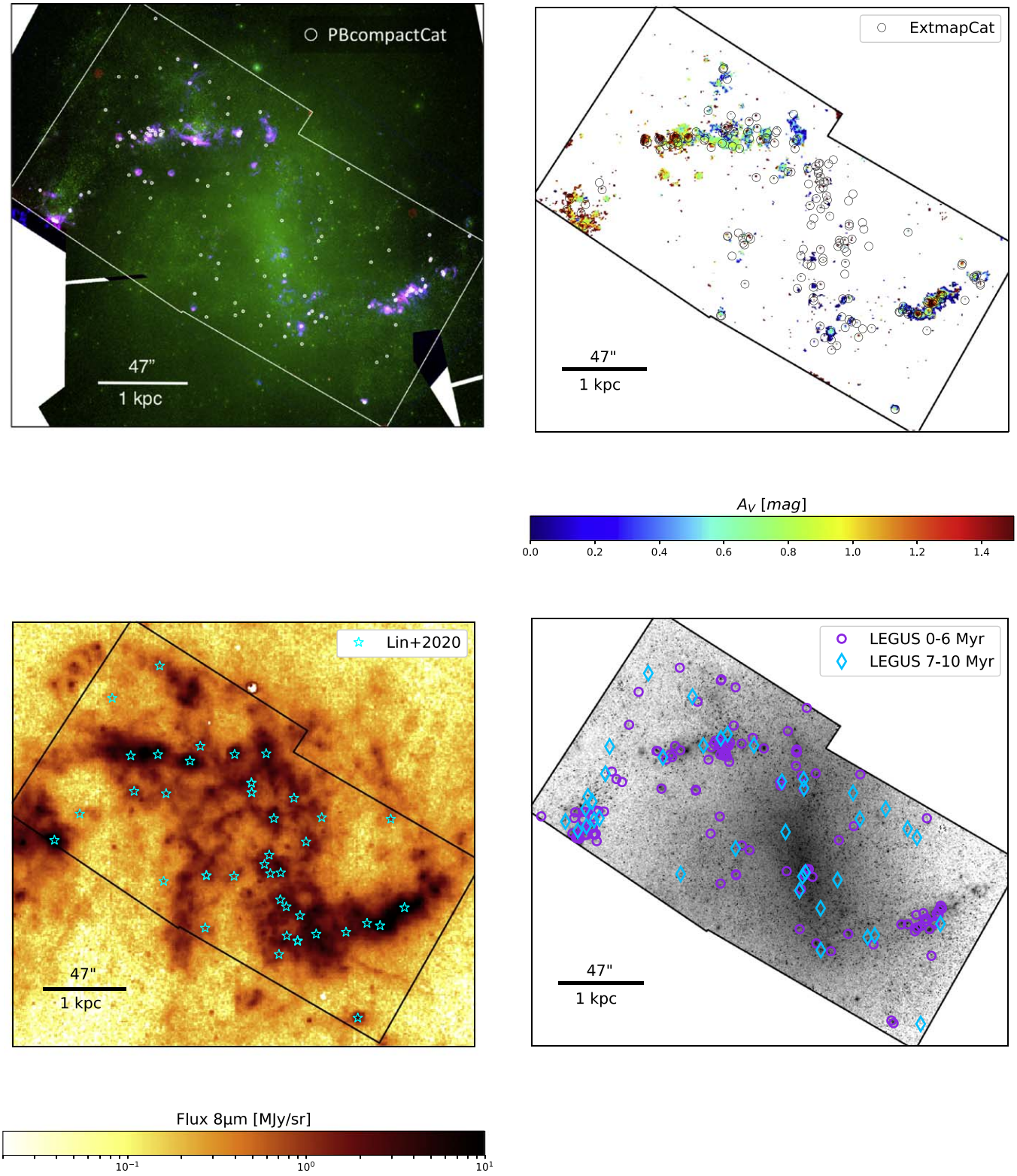

Figure 1. (Top left): RGB composite of NGC 1313 showing continuum-subtracted Hα in the blue channel, F555W in green, and continuum-subtracted Paβ in red. The coordinates of the sources from PBcompactCat are shown with white circles The thick white contour marks the field of view of the HST NIR observations. (Top right): map of the Hα/Paβ ratio, converted into an extinction map. The positions of the sources from the ExtmapCat are shown as black circles. (Bottom left): 8 μm emission from Spitzer, tracing the emission of the warm dust. We note that there is good spatial coincidence between the brightest 8 μm areas and the nebular extinction map. Cyan empty stars mark the position of the MIR sources studied in Lin et al. (2020). (Bottom right): the position of the cluster of the LEGUS catalog, divided into two age bins (0–6 Myr: purple circles, 7–10 Myr: blue diamonds), plotted over the F555W data. The age division is motivated by the analyses in Section 6.3. In each panel, a scale of 47″ (corresponding to 1 kpc) is given.

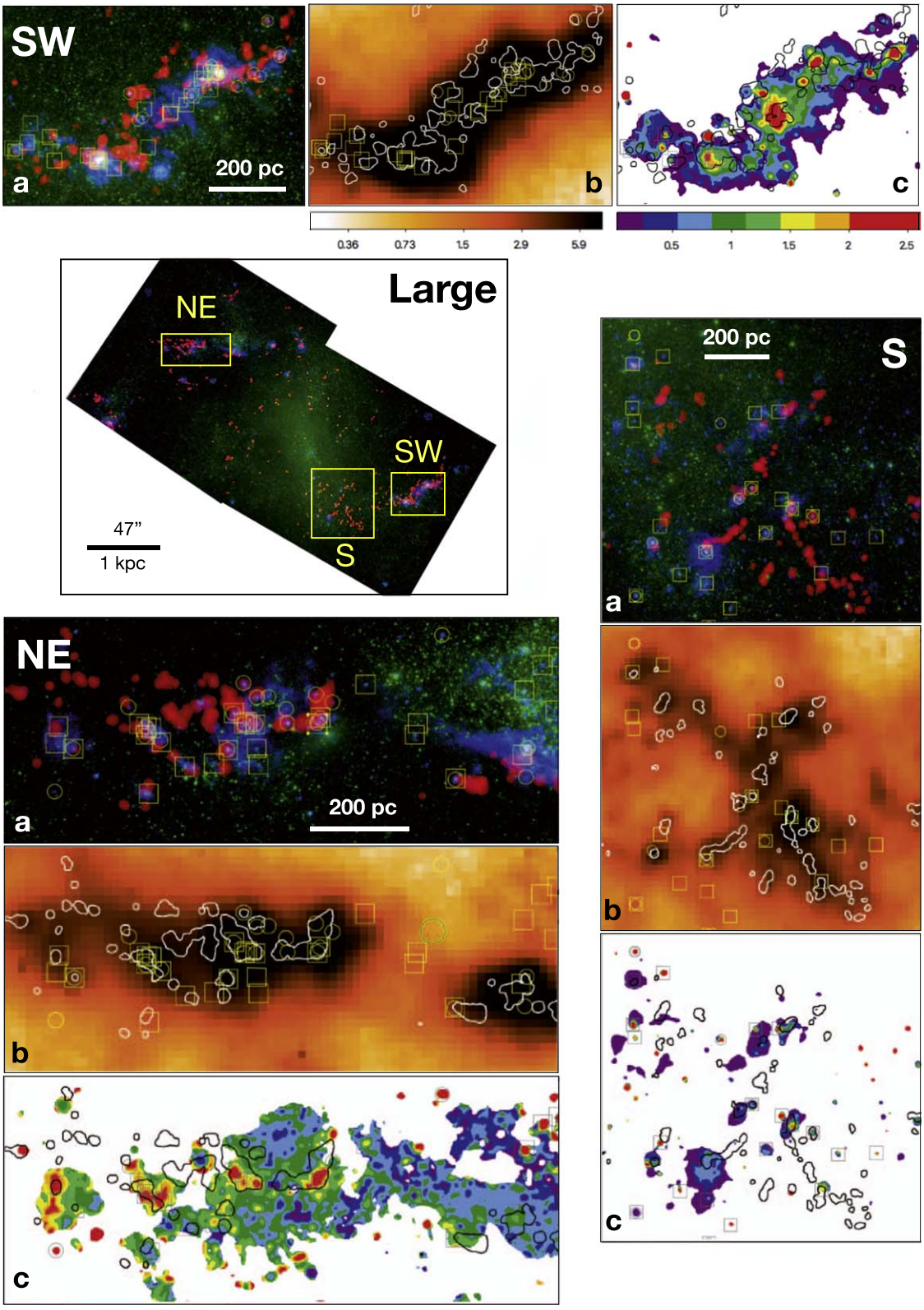

Figure 2. The “Large” panel shows Paβ (blue), V-band (green), and CO emission (red) for the entire galaxy. The other panels show multiband zoom-ins in three subregions (NE, S, and SW), including (a) the same RGB map as for the “Large” panel; (b) 8 μm emission from Spitzer (heat map, in units of MJy sr^{-1}), with CO contours overplotted in white; (c) a multicolored map showing the distribution of nebular extinction (in units of A_V[mag]), with CO contours overplotted in black. The scales of the 8 μm and extinction maps are the same in all panels. In all zoom-ins, the positions of sources in ExtmapCat and PBcompactCat are shown as empty squares and circles, respectively.

Previous studies of clusters in NGC 1313 in the NUV–optical found on average extinctions of $E(B-V)\sim 0.25$ mag ($A_V\sim 0.8$ mag) for young clusters. We aim to study clusters with higher extinction that may be missed in the NUV–optical bands. We therefore focus on the regions of the extinction map with $A_V \geqslant 0.8$ mag, and we visually select all the NIR sources with a clear counterpart in the F814W filter. We find a total of 188 cluster candidates. In the rest of the paper, we are referring

to this source catalog selected on the basis of the extinction map as ExtmapCat. We plot the positions of the sources within the galaxy in Figure 1 (top-right panel).

3.2. Sources with Compact Paschen-β Emission

In order to search for sources not detected in Hα but emitting in Paβ, and therefore missed by the extinction map (limited by the Hα detection), we select a second catalog of sources. From the continuum-subtracted Paβ map described previously, we select sources with detectable (S/N > 3) Paβ compact emission (i.e., with a narrow light profile, consistent with that of stars and clusters, avoiding diffuse emission). This approach helps to detect embedded sources that have Paβ detection but may be missed in Hα; this catalog and ExtmapCat are complementary, as they can overlap but are not mutually exclusive.

We retrieve 124 sources with compact Paβ emission, and for the rest of the paper, we refer to this catalog as PBcompactCat. Of these, 40 are in common with the ExtmapCat. We plot the coordinates of the sources in this second catalog in Figure 1 (top-left panel). While many sources reside in the extended regions of recent star formation outlined previously, some Paβ-compact sources reside outside the main spiral arms.

In the same Figure 1, we compare the position of sources in our catalogs with the position of MIR compact regions, selected in Spitzer 8 μm observations by Lin et al. (2020). We remind readers that 8 μm observations have a much lower resolution than the HST one, and that sources in the Lin et al. (2020) catalog were selected to have some HST cluster counterpart. Overall, the different catalogs cover similar regions of the galaxy; however, some of the Lin et al. (2020) sources are not present in our catalogs. In Figure 2, we compare the spatial position of the nebular emission and 8 μm emission with CO clouds found by ALMA (details on the data and of their analysis will be presented in a forthcoming paper, M. K. Finn et al. 2021, in preparation), focusing on three subregions of the galaxy. Also, CO emission (which traces the GMCs) has a good spatial coincidence with 8 μm emission and regions of elevated nebular extinction, with some visible exceptions; in the SW portion of the spiral arms, some CO clouds are displaced from the peak of nebular emission, suggesting the presence of gas which is still dark in NIR. The S region is instead mostly missed by the extinction map, or presents only low extinction values, A_V <0.5 mag, despite the presence of both CO and 8 μm emission. A possible cause is that the entire S region is in a very early phase of star formation, still invisible even in the NIR bands. This multiband comparison shows how, while the sources extracted in ExtmapCat and PBcompactCat are distributed across the entire galaxy, some regions of early star formation may still be so obscured to be inaccessible in the HST NIR bands.

We point out that sources in both ExtmapCat and PBcompactCat were included in the catalogs without a detailed morphological classification; the two catalogs may therefore contain interlopers, such as bright stars. Photometry and size analyses are performed on all the sources (in Section 4), and their results will be used in Sections 5.1 and 5.2 to clean the samples, producing final catalogs.

3.3. LEGUS Catalog

In the course of the current paper, we will discuss our results in light of the results achieved by the study of the cluster catalog of NGC 1313 obtained by the LEGUS project. Such catalog was used to study the hierarchical distribution of young clusters (Grasha et al. 2017a, 2017b), the distribution of their sizes (Ryon et al. 2017), and the typical evolution timescale associated with their H II regions (Hannon et al. 2019).

The methodology used to extract cluster catalogs in LEGUS is fully described in Adamo et al. (2017), and we direct the interested reader to that work for the details. We report here only a few main points, relevant for the current work. The LEGUS cluster catalog of NGC 1313 was built upon five broadband filters, covering the *NUV*, *U*, *B*, *V*, and *I* bands. The optical data are the same used by this current analysis. In addition, we used the data in the filters F675N and F546M already presented in Hannon et al. (2019). Ages and masses were derived via spectral energy distribution (SED) fitting of the five mentioned optical broadbands only for cluster candidates brighter than $M_V = -6$ mag in the *V* band and with photometric detections in at least four of the bands. A visual morphological classification was used to separate centrally concentrated clusters from multipeaked compact associations and to separate out contaminating sources (foreground stars, background galaxies, etc...) picked up by the initial source extraction. The spatial distribution of the clusters from the LEGUS catalog within the galaxy is shown in Figure 1 (bottom-right panel).

4. Analysis

At variance with the standard LEGUS SED analysis, we use in this work the information produced by the combined 10 bands of photometry from NUV to NIR (Section 4.1) to estimate ages, extinctions, and masses of the sources in our catalogs (Section 4.3). We also use Paβ and Hα equivalent width (EW) measurements as an independent way to estimate cluster ages (Section 4.4).

4.1. Photometry

For all the catalogs, we use a standard aperture photometry approach, using circular apertures with radii of 0.″16 (4 px in the optical filters, 2 px in the NIR ones) in all bands. The sky background is estimated in an annulus centered on the source with radii of 0.″20 and 0.″28 by taking a clipped[11] median. The value of the sky is then normalized by the area in the circular aperture and subtracted from the flux. Previous to the photometry, each source is centered using a centroid algorithm in the F814W filter, and its coordinates are then kept fixed in all the other bands. We used F814W as a reference because it is the reddest optical filter in our set. The NIR filters have an instrumental PSF that is roughly twice as large (in arcsec) compared to that of the optical filters. Optical filters are therefore fundamental to discriminate multiple sources, i.e., separated by less than a few pixels transverse to the line of sight.

An aperture of 0.″16 in radius includes ∼80% of the flux for PSF-like light profiles, and this fraction decreases for wider light profiles. We apply an aperture correction to account for this missing flux. We consider as total flux the one enclosed in a circular aperture with a radius of 0.″8. In order to estimate the aperture correction, we convolve the instrumental PSF[12] of each filter with a Moffat profile (Elson et al. 1987), considered the most accurate function to describe the light profile of clusters (e.g., Elson et al. 1987; Bastian et al. 2013). We take as the reference value for the aperture correction the one obtained from a Moffat profile with an effective radius $R_{\rm eff} = 2.5$ pc, as the distribution of cluster sizes is peaked at that value (Ryon et al. 2015, 2017).

[11] The clipping avoids considering pixels more than 3σ above the mean of the pixel values in the annulus. This helps eliminate sources from the background estimate.

[12] Obtained from isolated stars in the data.

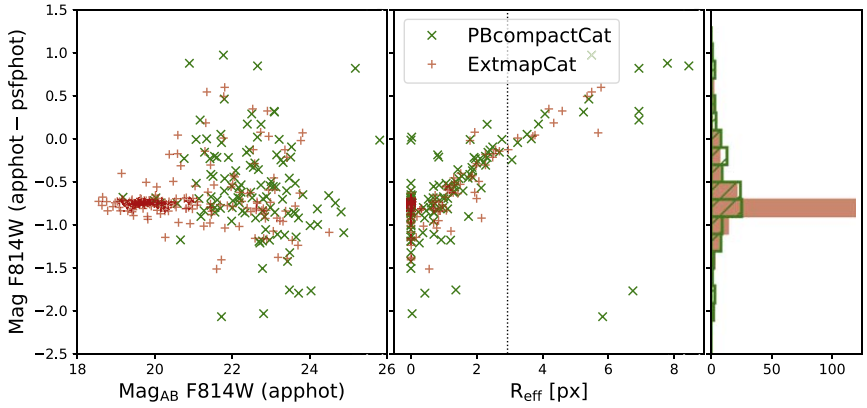

Figure 3. Comparison between the photometry in the F814W filter obtained via the aperture photometry process (apphot) and via the alternative size-photometry (psfphot) as a function of the F814W photometry itself (left panel) and of the recovered effective radius, $R_{\rm eff}$ (central panel). The distribution of the photometry differences (right panel) shows a peak around 0.8 mag, due to the presence of many sources with PSF-like light profiles. The black dotted vertical line in the central panel marks $R_{\rm eff} = 2.9$ px, corresponding to the value $R_{\rm eff} = 2.5$ pc used as a reference for estimating the average aperture correction (see Section 4.1).

Different choices of the aperture correction would change the normalization of the fluxes, but not the shape of the SED. In the context of broadband SED fitting, they would have an effect only on the recovered masses, leaving unchanged ages and extinctions. We discuss different choices of aperture corrections in Section 6.1.

The radius of the photometric aperture was chosen as a compromise between including most of the sources' fluxes within the aperture and avoiding contamination from nearby sources. Nevertheless, some of the sources suffer from contamination from the light of nearby sources. We consider as contaminated the cases where, within an aperture, the flux of nearby sources contributes at least $\sim 1/3$ of the total. Sixty-one sources (out of 188, i.e., 32%) of the ExtmapCat have contamination in at least 1 filter, while for the PBcompactCat catalog, the same is true for 16 sources (out of 124, i.e., 13%). Most of the contamination takes place in the bluer bands of our filter set, especially in the F275W and F336W filters. The source selection, focused on the red-optical and NIR filters can be a possible cause; many sources of the catalogs are bright in the red filters, but their flux in the blue part of the spectrum appears dim and therefore more easily contaminated by nearby sources.

4.2. Cluster Sizes and Alternative Photometry

The size of stellar clusters in NGC 1313 was studied in detail in Ryon et al. (2017). The authors showed that the concentration index, CI (defined as the magnitude difference in circular apertures of 1 px and 3 px radii), is able to reproduce the overall distribution of sizes derived by more detailed means such as the software `GALFIT`. The advantage of using a such a simple metric is that it does not require any supervision and therefore produces reliable results quickly. One possible limitation of the size estimates given by the CI is the presence of crowding, where nearby sources can greatly affect the measure of the CI.

In order to overcome this problem, we implement an alternative measure of the sizes by performing a 2D fitting of the source. This method builds upon the size-photometry script described in Messa et al. (2019); we model the source with the stellar PSF convolved with a Moffat profile, normalized by the flux, and summed to a first-degree polynomial that models the sky background. From each source, we produce a cutout of the F814W data of 11×11 px size that we fit, comparing it to the source model via a Levenberg–Marquardt minimization. This method was tested to be ineffective in discriminating sizes smaller than $R_{\rm eff} = 0.69$ px (corresponding to $R_{\rm eff} = 0.59$ pc at the distance of NGC 1313). We therefore consider all sources with $R_{\rm eff} \leqslant 0.69$ px as consistent with having a stellar PSF.

We use the size-photometry method just described to also perform a complementary photometry. In this case, we do not rely on an (average) aperture correction, and the results are used to provide an estimate of the total flux of the clusters based on their sizes. For each source, we keep fixed the central coordinates and the size retrieved in the F814W filter and then we repeat the Levenberg–Marquardt minimization in all other filters, leaving only the flux (and the parameters describing the background) as free parameters. More details on this method are given in Appendix A. The photometric results obtained in this way are used in Section 6.1 to discuss the mass distribution of the cluster catalogs.

The comparison between the photometry obtained with this method and the one obtained via the aperture photometry analysis described in Section 4.1 is shown in Figure 3. There is a magnitude offset of $\sim$0.8 mag, especially clear for the ExtmapCat sources. This offset is caused by the aperture photometry method having a fixed aperture correction (calibrated on a typical cluster size, see the previous section) as opposed to the size-photometry method. The right panel of Figure 3 shows how the offset decreases when increasing estimated source sizes, being null at $R_{\rm eff} \sim 2.5$ pc. Combining the information from the two panels in Figure 3 we notice that the offset is mostly caused by bright sources with narrow profiles; these are probably stars and are excluded from the final samples (see Sections 5.1 and 5.2). The same sources drive the narrow scatter of the distribution for the ExtmapCat compared to the PBcompactCat. Finally, the large overall scatter of the magnitude difference between the two methods (going from -2 to $+1$ mag) can be simply explained by the different sizes of the sources considered. When focusing on the sources at a fixed estimated size, the scatter reduces considerably (Figure 3, central panel).

4.3. SED Fitting

We perform a least-χ^2 fitting of the broadband SED obtained from the photometry in Section 4.1, following a very similar approach to the one used in LEGUS (see Adamo et al. 2017). We use as spectral models the Yggdrasil single-stellar population (SSP) models[13] (Zackrisson et al. 2011). In detail, we use the modes created from the Starburst99 Padova-AGB tracks

[13] Available at https://www.astro.uu.se/~ez/yggdrasil/yggdrasil.html.

(Leitherer et al. 1999; Vázquez & Leitherer 2005) with a universal Kroupa (2001) initial mass function (IMF) in the interval 0.1–100 $M_{\odot}$. These models assume that the IMF is fully sampled. The stellar models are then used as input to run Cloudy (Ferland et al. 2013) and to obtain the evolution of the nebular continuum and line emission, produced by the ionized gas surrounding the young clusters. Yggdrasil adopts a spherical gas distribution around the emitting source, with hydrogen number density $n_{\rm H} = 10^2$ cm^{-3} and gas filling factor (describing the porosity of the gas) $f_{\rm fill} = 0.01$, typical of H II regions (Kewley & Dopita 2002), and assumes that the gas and the stars form from material of the same metallicity. We consider a subsolar metallicity ($Z = 0.008$) for NGC 1313 as it results in a best fit of the young clusters but we also test models with solar ($Z = 0.020$) metallicity (see discussion in Section 5.1.1 and the figures in Appendix B). We choose the models with a gas covering fraction $f_{\rm cov} = 0.5$, i.e., only 50% of the Lyman continuum photons produced by the central source ionize the gas. While Yggdrasil provides multiple choices for $f_{\rm cov}$, we decide to keep it fixed, as it reasonably describes the case of ionized and partially leaking nebulae around young star clusters. Including the nebular emission in the cluster models is fundamental, and omitting it would lead to misleading results (Zackrisson et al. 2001; Adamo et al. 2010; Reines et al. 2010). Nevertheless, we do not have enough information to disentangle the gas conditions from our fitting process. We tested fitting the sources using models with $f_{\rm cov} = 1.0$ i.e., no leakage of LyC photons, finding no substantial difference in the distribution of recovered cluster ages, masses, and extinctions. We therefore kept models with $f_{\rm cov} = 0.5$ as the reference one in our analysis.

Starting from the Yggdrasil models, we create a grid for the fitting by combining the spectra at progressive age steps and increasing internal reddening. We keep the same age steps included in Yggdrasil, which provides a 1 Myr interval frequency in the range [1; 15] Myr. The sampling decreases at older ages but we are not affected by it, as we are interested in the very young sources. The models are reddened prior to being fitted using a foreground dust geometry with a grid of extinctions in the range $E(B-V) = [0.0; 2.5]$ mag with a step of 0.01 mag. This is the only difference from the LEGUS approach, which used a grid of extinction extending only up to $E(B-V) = 1.5$ mag. We use as reference the Milky Way extinction law (Cardelli et al. 1989) but, as a test of the robustness of the results from our fit, we also consider the differential (i.e., the gas emission suffers higher extinction than the stars) starburst attenuation law (Calzetti et al. 2000). The fitting is done using a traditional χ^2 approach on the grid just described. The model spectrum is normalized for each age–extinction combination in order to minimize the reduced χ^2 ($\chi^2_{\rm red.}$), for every source. The best fit for a source is given by the combination of age–extinction that minimizes the $\chi^2_{\rm red.}$ value. An uncertainty interval is given for the best-fit parameters by considering all the sources within 1σ from the best-fit values, i.e., the parameters that result in a $\chi^2_{\rm red.}$ within 3.53 from the minimum $\chi^2_{\rm red.}$.

Some of the sources in our catalogs have large photometric errors, while some others are contaminated, in some filters, by the emission of nearby sources, as described in Section 4.1. We decide to exclude from the fit the cases where the photometric uncertainty is above 0.3 mag (i.e., S/N <3), as sources with an uncertainty above that level have only a partial detection. We also exclude from the fit the cases of contamination, as their photometry would lead to misleading results. We fit the sources where at least five bands are left after the uncertainty–contamination cut, for a total of 170 sources for the ExtmapCat and 98 sources in the case of the PBcompactCat. The results of the fitting process are shown and described in Section 5.

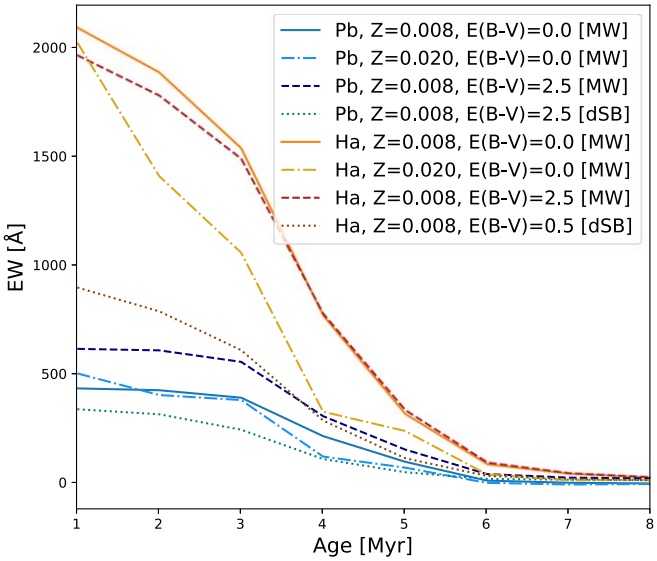

Figure 4. Equivalent widths of Hα (red/yellow colors) and of Paβ (blue colors) as a function of cluster ages, as measured from the models convolved with the filters used for the fit. Different combinations of metallicity and extinction curves are given (see legend).

4.4. Hα and Paβ Equivalent Width Analysis

A direct way of deriving the age of a cluster is to use the EWs of the nebular emission lines, defined as

$$\mathrm{EW}_{\lambda} = \int \frac{F_{\rm obs}(\lambda) - F_c(\lambda)}{F_c(\lambda)} d\lambda, \quad (3)$$

where $F_{\rm obs}(\lambda)$ is the observed flux across the emission line at the wavelength λ, and $F_c(\lambda)$ is the continuum level underneath the emission line. We do not have spectra of our sources, and we therefore have to rely on a combination of broad and narrow filters to estimate the EW. Similarly to what was done in Section 3.1, we use the filters adjacent to the narrow one containing the line to estimate the continuum. For $\mathrm{EW}_{\rm H\alpha}$, we use a logarithmic interpolation of the fluxes in the F547M and F814W filters to find the flux of the continuum emission at the pivotal wavelength of the F657N filter, $F_{C,\rm H\alpha}$. We calculate the flux in the Hα line by subtracting $F_{C,\rm H\alpha}$ from the total flux measured in F657N, $F_{L,\rm H\alpha} = F_{\rm F657N} - F_{C,\rm H\alpha}$. From Equation (3), we derive in our case

$$\mathrm{EW}_{\rm H\alpha,obs} = \frac{F_{L,\rm H\alpha}}{F_{C,\rm H\alpha}} \cdot \mathrm{BW}_{\rm F657N}, \quad (4)$$

where $\mathrm{BW}_{\rm F657N} = 122$ Å is the width of the narrowband filter.

In a similar way (using $\mathrm{BW}_{\rm F128N} = 157$ Å as the width of the narrow Paβ filter), we derived EW(Paβ) using F110M and F160W to estimate the continuum $F_{C,\rm Pa\beta}$ and consequently to measure the Paβ line emission at $F_{L,\rm Pa\beta} = F_{\rm F128N} - F_{C,\rm Pa\beta}$, after using the iterative procedure for the F110W described in Section 3.1.

We use the SSP models described in the previous section to estimate the EW expected at different cluster ages. The EW values that we measure depend on our specific set of filters, and therefore, we cannot rely on theoretical values; we prefer instead to use directly the models to create a comparison set for the data. Figure 4 shows the evolution of the Hα and Paβ EWs with the

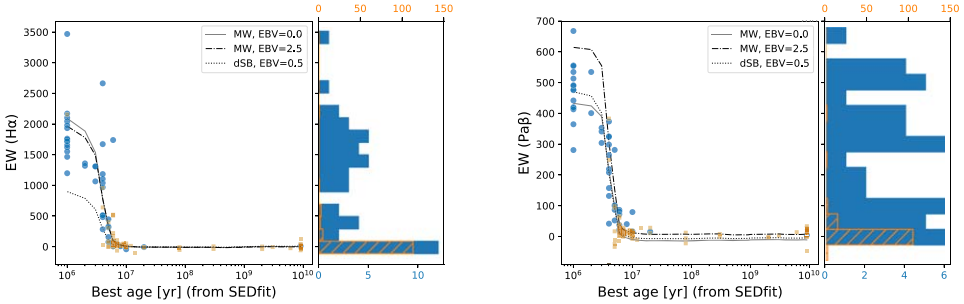

Figure 5. Distribution of estimated Hα (left panel) and Paβ (right panel) equivalent widths and best-fit age values for the ExtmapCat sources. The sample is color-coded according to the light profile being either PSF-like ($R_{\rm eff}\leqslant$0.59 pc, orange) or larger ($R_{\rm eff}>$0.59 pc, blue). The solid, dashed–dotted, and dotted lines are the expected trends, see Figure 4.

age of the clusters for different metallicities and extinctions. From the definition in Equation (3), the EW should not be affected by extinction, if lines and continuum are extincted in the same way. However, because we have to rely on a combination of broad and narrow filters, we see the measured EW being slightly different (typically <10%) at very young ages ($\leqslant$3 Myr) for different extinction values. Differential Starburst extinction is the one with the largest impact, acting more severely on the lines, $E(B-V)_{\rm star}=0.44\cdot E(B-V)_{\rm gas}$ (Calzetti et al. 2000), as can be appreciated from Figure 4.

4.5. Completeness Test

We study the completeness of our samples, both in terms of photometry and SED fitting. We built a control sample of sources with preset ages and masses, adding them to the observational data and going through the entire process of photometric analysis and SED fitting to recover their properties. We fix the sizes of the sources at $R_{\rm eff}=1$ px and the masses at $M=10^3\,M_\odot$; these values, according to the results of our analysis presented in Sections 5.3 and 6.1, are reasonable assumptions. We simulate 100 sources for each combination of ages in the age range [1; 6] Myr with steps of 1 Myr and of extinctions in the range [0; 2] mag with steps of 0.25 mag, for a total of 30 combinations (3000 simulated sources). The galaxy is divided into grids of size $4''\times4''$, and the simulated sources are located only in cells where at least one source from ExtmapCat or PBcompactCat is found. In this way, we measure completeness in the same regions where the real data are located. Only 100 sources per time are inserted in the data frames, in order to avoid biasing the photometry due to overcrowding.

We perform aperture photometry on the entire sample of simulated clusters; almost all of them have photometric uncertainties below 0.3 mag (S/N > 3) for all ages and extinctions, in both F814W and F128N, the two filters used as the reference ones for the source extraction (the exact number is collected in Appendix C). We deduce that we are complete in the detection of the catalog up to a level between 90% and 100%. Most of the simulated sources have photometric uncertainties below 0.3 mag in at least five filters and are therefore fitted. Appendix C gives the exact number of such sources, at each age and extinction; their fraction stays around $\sim$90% for sources up to extinctions of $E(B-V)=$ 1.5 mag. For higher extinctions, it decreases and strongly depends on the age.

We discuss in Section 6.2.1 the accuracy we have on the simulated clusters in retrieving the input ages and extinctions.

5. Results

5.1. Ages, Extinctions, and Masses of ExtmapCat

We show in Figure 5 the best-fit age values of the sources in the ExtmapCat, along with their Hα and Paβ EW values; we color-code the sources according to their size, separating the ones with a light profile consistent with the instrumental PSF ($R_{\rm eff}\leqslant$0.59 pc in the F814W filter), and therefore possibly stars, from those with a larger size ($R_{\rm eff}>$ 0.59 pc). Overall, we find a good consistency between the ages derived from the SED fit and what could be expected from the EW values. We do not find sources with age >8 Myr with high EW in either Hα or Paβ, confirming the general robustness of our fitting procedure. The largest differences of the EW values from the ones predicted (in Section 4.4) are at the youngest ages of 1 Myr, possibly caused by an inaccuracy in the derived ages. Confirming this hypothesis, we show in Appendix C how ages in the range 0–3 Myr are degenerate. If, instead of the Milky Way extinction curve, we assume the differential starburst one, predictions and observations remain consistent with each other (see Figure 5).

In Figure 6, we show the same best-fit ages along with extinctions (left panels) and masses (right panels), and their uncertainties. We notice that the sources cover, unevenly, the entire age range considered in the model grids. We, however, point out that almost all of the sources falling in the last age bin considered (age $\sim$10 Gyr) have a PSF-like light profile, consistent with being stars. Their masses are on average very high ($>10^5\,M_\odot$), but this is caused by considering them as very old and mildly extincted clusters. Most of the sources with the best age between $\sim$10 Myr and $\sim$10 Gyr have large uncertainties, covering hundreds of Myr. Many of the sources are aggregated around $\sim$10 Myr of age and elevated extinction values; this overdensity can be due to degeneracies in the models causing artificial high extinction estimates. In particular, low-mass (of several hundred $M_\odot$) old clusters hosting luminous bright late-type stars and therefore appearing "red" (bright in the F814W and redder filters) can be misclassified as young ($\sim$10 Myr and younger) and extincted clusters, as pointed out e.g., in Hannon et al. (2019).

In order to clean the catalog from sources with unconstrained properties, we leave out the sources with age uncertainties $\Delta\log_{10}(\text{age})>1.5$. In this way, all the sources with an age uncertainty covering almost the entire range from $\sim$10 to $\sim10^4$ Myr are discarded (see the comparison between the top and bottom panels in Figure 6). We also leave out of the final sample most of the stellar-like sources; among the sources with $R_{\rm eff}<$0.59 pc, we keep only those with Hα and Paβ EW consistent with having ages $\leqslant$5 Myr (i.e., with values of 317 Å and 95 Å in the case of Hα and Paβ, respectively). We show the

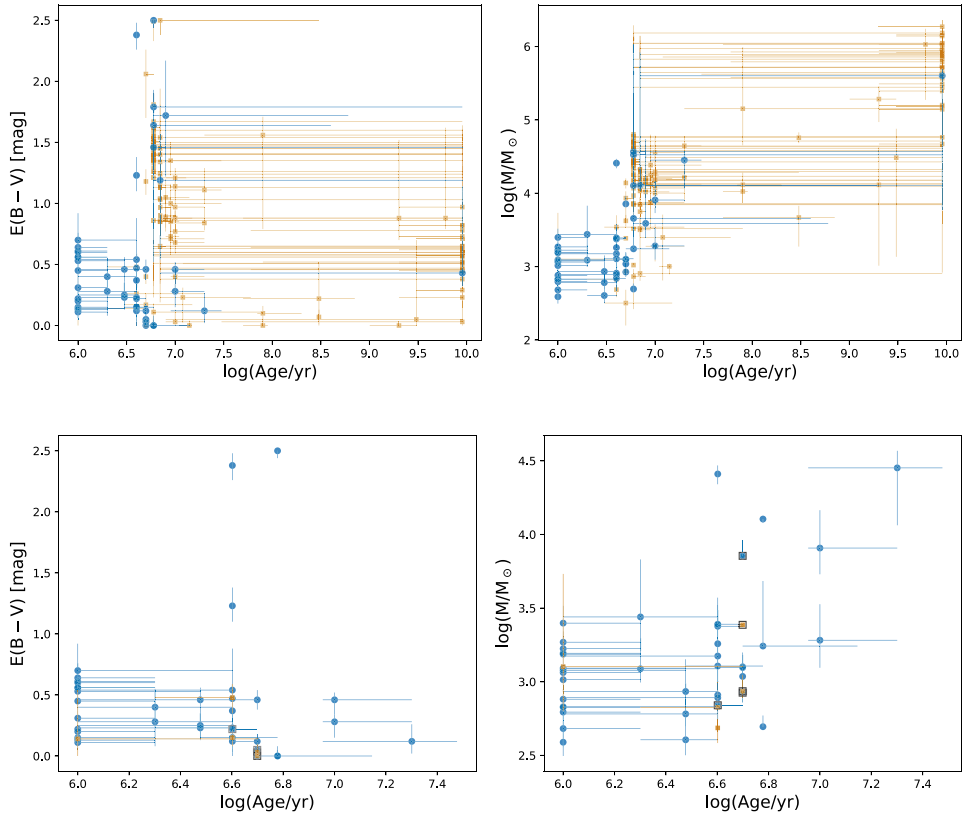

Figure 6. Ages, extinctions (left panels), and masses (right panels) of the ExtmapCat, as derived from the broadband SED fit. The sample is color-coded according to the light profile being either PSF-like ($R_{\rm eff}$ ⩽0.59 pc, orange) or larger ($R_{\rm eff}$ >0.59 pc, blue). The bottom row shows the results for the final selection of the sample (ExtmapCat-final); see main text. Empty black squares in the bottom plot are used for the five sources with blue SED, typical of young sources, but no line emission. The scale of the *X*-axis in the bottom-row plots was adapted to the narrower range spanned by the data in the final sample.

Table 2
Summary of the Number of Sources in the Initial Extracted Samples (ExtmapCat and PBcompactCat, Section 3) and in the Final Samples (ExtmapCat-final and PBcompactCat-final, after the Selection Described in Section 5.1)

	ExtmapCat	PBcompactCat
Total	190	124
Stellar	136 (72%)	39 (31%)
Resolved	54 (28%)	85 (69%)
	ExtmapCat-final	PBcompactCat-final
Total	46	84
Stellar	5 (11%)	13 (15%)
Resolved	41 (89%)	71 (85%)
In common	30	

remaining sources in Figure 6 (bottom panels). This final selection (ExtmapCat-final) counts 46 sources as reported in Table 2. The coordinates and best-fit properties of the clusters included in the final catalog are listed in Table 3.

The recovered masses are mostly distributed in the range [300; 3000] $M_\odot$ (Figure 6, right panels). Sources with masses below ∼1000 $M_\odot$ can be expected to have an uneven sampling of the stellar IMF. This could cause the absence of massive stars able to ionize the gas surrounding the cluster, and, as a consequence, the absence of line emission in our photometry. From a visual inspection of the broadband SEDs of our sample, we find that only five sources in the entire ExtmapCat sample are consistent with having an SED typical of very young (age ⩽6 Myr) clusters but show no or little line emission in Hα and Paβ.[14] The low number of clusters suffering from the lack of ionizing stars, despite the low range of masses recovered, could suggest an underestimation of the masses, due to a poor choice of the average aperture correction values. We discuss this possibility in Section 6.1.

We show the position of ExtmapCat-final sources within the galaxy in Figure 7. They are all located in regions of recent star formation, mainly along the arms of the galaxy. Conversely, the sources discarded from the final selection are more scattered along the entire galaxy, confirming the reliability of our criteria in selecting young clusters.

Only three young sources with extinctions $E(B-V)$ >1.0 mag remain after the selections. We show the distribution of their $\chi^2_{\rm red.}$ from the fitting analysis, along with the broadband SED in Appendix B. Two of them (C93 and C142) have high values for the best-fit $\chi^2_{\rm red.}$, ($\chi^2_{\rm red.} > 20$). C10 is the best candidate for being young and highly extincted, with $E(B-V) = 1.23$ mag.

5.1.1. Testing Metallicities and Extinction Laws

We performed the SED fit by varying some of the model parameters, namely the metallicity and the extinction law. In order to better display the distribution of the sources in the age–extinction plane, along with their uncertainties, we use a density plot, based on a fixed grid of ages and extinction

[14] Despite the lack of compact line emission, such sources have been selected in the ExtmapCat sample because they are located in regions of diffuse nebular emission.

Table 3
Catalog of Detected Sources Included in the Final Cluster Samples (*E*xtmapCat-final and PBcompactCat-final)

ID	R.A.	Decl.	$R_{\rm eff} \pm$ err	Age	A_m	A_M	$E(B-V)$	E_m	E_M	log(Mass)	M_m	M_M	$\chi^2_{\rm red}$	Cat.
C2	49.63122	−66.47942	1.70 ± 0.05	3	1	4	0.46	0.36	0.56	2.78	2.69	2.99	4.8	EP
C3	49.62640	−66.47905	2.12 ± 0.10	1	1	2	0.64	0.52	0.76	2.68	2.55	2.81	6.4	EP
C4	49.62534	−66.47924	0.72 ± 0.04	1	1	4	0.70	0.57	0.92	2.83	2.68	3.06	9.1	EP
C5	49.62634	−66.47883	0.81 ± 0.06	4	4	4	0.47	0.39	0.55	3.26	3.16	3.36	5.9	EP
C9	49.62049	−66.47846	1.00 ± 0.03	1	1	2	0.61	0.55	0.68	3.22	3.15	3.31	6.7	EP
…	…	…	…	…	…	…	…	…	…	…	…	…	…	…

Notes. Column (1): cluster ID number. Columns (2) and (3): R.A. and decl. coordinates in decimal degrees (J2000). Column (4): effective radius and its uncertainty, in units of parsec. Columns (5), (6), and (7): best-fit age with minimum (A_m) and maximum (A_M) values within 1σ, in units of Myr. Columns (8), (9), and (10): best-fit $E(B-V)$ with minimum (E_m) and maximum (E_M) values within 1σ, in units of mag. Columns (11), (12), and (13): best-fit logarithmic mass with minimum (M_m) and maximum (M_M) values within 1σ, in units of $M_\odot$. Column (14): reduced χ^2 of the SED fit. Column (15): catalog containing the cluster: "E" stands for ExtmapCat-final, "P" stands for PBcompactCat-final, while "EP" means that the source is contained in both final catalogs.

(This table is available in its entirety in machine-readable form.)

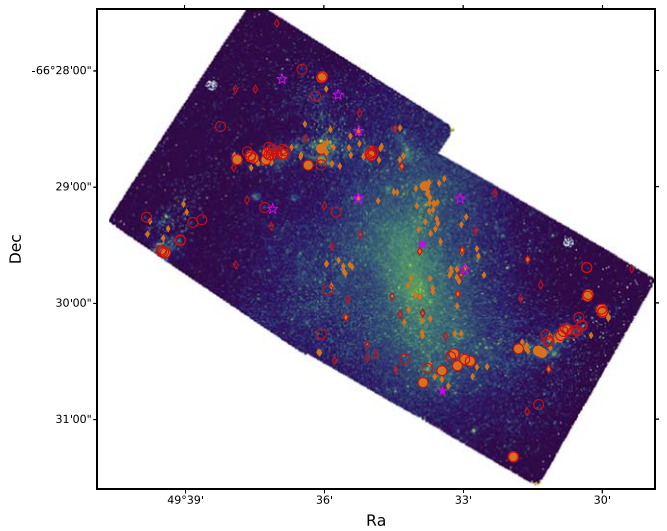

Figure 7. Distribution of the sources of the ExtmapCat (orange filled diamonds) and PBcompactCat (red empty diamonds). The clusters in the final samples have been marked by filled orange circles and empty red circles for the respective catalogs. The positions within the galaxy are plotted over the F128N image data. The clusters from the final catalogs with derived extinctions $E(B-V) > 1.5$ are marked by magenta stars (filled for ExtmapCat, empty for PBcompactCat) and are discussed in Section 6.2.2.

intervals (Figure 8). Each source is considered to cover all cells in the grid included within its upper and lower limits (both in age and $E(B-V)$ values) as given by the face value $\pm$ the uncertainty. Its value in such cells is normalized by the number of the cells covered; in this way, the final sum of the cell values over the entire grid is equal to the total number of sources considered. We use a grid with a 1 Myr step in ages in the range [1; 10] Myr and a with a step of 0.25 mag in the $E(B-V)$ range [0.0; 2.5] mag.

We consider SSP models with solar metallicity for the fit and select a final sample in the same way as described in the previous chapter. The final sample counts the exact same sources as in ExtmapCat-final. We compare the recovered ages and extinctions using the density plot in Figure 8 (central panel). On average, solar-metallicity models recover slightly older and more extincted sources. The median $\chi^2_{\rm red}$ recovered with the solar-metallicity models is higher than the one of the reference sample (Figure 9, left panel). An inspection of individual sources' SEDs confirms that subsolar models provide a better fit to the photometry; photometric data containing strong emission lines show an abrupt increase of the flux in the filter F555W compared to F547M, despite their pivot wavelength being very similar. This difference is caused by different bandwidths, allowing F555W to include strong emission lines such as O[III], in contrast to F547M. Different metallicities for the stellar models imply different strengths for the nebular lines and therefore different predicted fluxes, as shown for some examples in Appendix B. We conclude that the availability of both F555W and F547M filters allows us to disentangle the model metallicity that gives a better agreement with the data, in this case subsolar, $Z = 0.008$.[15]

We repeat all the analyses, including the final selection, using subsolar metallicity models but implementing a differential starburst attenuation. The final sample selected remains almost identical to the reference ExtmapCat-final. The most notable difference is the presence of two additional sources as young extincted cluster candidates, C33 and C175, whose $\chi^2_{\rm red}$ distributions and best-fit fluxes are collected in Appendix B. The distribution of ages and extinctions shown in the density distribution plots in Figure 8 reveals little difference from the reference case. On average, starburst extinction models recover younger and less extincted sources. The median $\chi^2_{\rm red}$ recovered in this case is slightly larger than in the reference case (Figure 9, right panel).

5.2. Ages, Extinctions, and Masses of PBcompactCat

We show in Figure 10 the best-fit age values for the sources in the PBcompactCat, along with the EW of Hα and Paβ, comparing them to the EW from the models, again color-coding them according to their light profile (red for stellar-like, green for larger). As in the previous sample, we find good consistency between the ages derived from the SED fit and Hα and Paβ EW values. We note that there are no sources with EW(Paβ) $\sim$0, because of sample selection criteria. For the same reason, most of the sources with PSF-like light profiles have large Hα and Paβ equivalent widths.

We show in Figure 11 the best-fit values of ages, extinctions, and masses, along with their uncertainties. The great majority of sources cluster around ages smaller than 10 Myr; we attribute this to the selection method of the sample, based on the observation of compact nebular emission and therefore biased toward young sources. We implemented the same

[15] No observable difference was observed if a metallicity $Z = 0.004$ was considered.

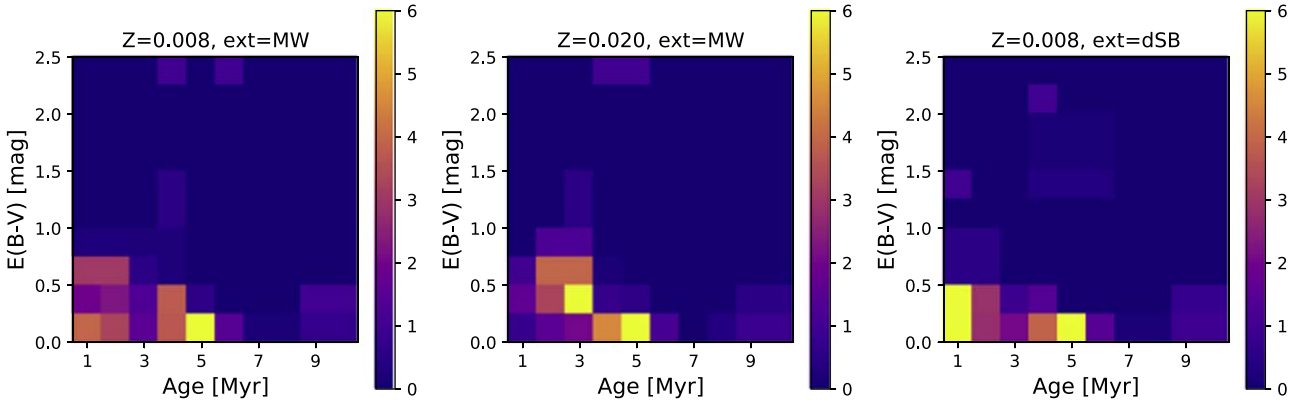

Figure 8. Density plots for the ExtmapCat-final sources, showing their distribution in the age–extinction plane. The different panels refer to the results using subsolar metallicity and Milky Way extinction (left), solar metallicity and Milky Way extinction (center), and subsolar metallicity and differential starburst extinction (right).

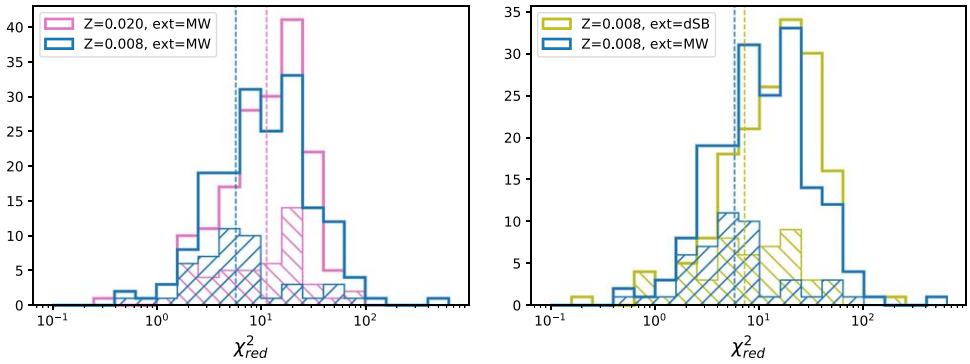

Figure 9. Distribution of the $\chi^2_{\rm red.}$ values from the best-fit results. Empty histograms refer to the total ExtmapCat sample, hatched histograms to the ExtmapCat-final sample. Vertical dashed lines are median $\chi^2_{\rm red.}$ values of the final samples, namely 5.8 for Milky Way extinction with $Z = 0.008$, 11.4 for $Z = 0.020$, and 7.2 for differential starburst extinction.

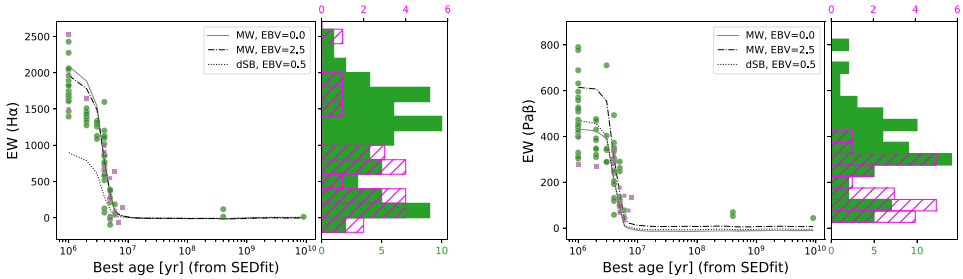

Figure 10. Same as Figure 5, but for the PBcompactCat sources. Orange has been changed into magenta, blue into green.

selection criteria used for cleaning the ExtmapCat, reaching a final sample (PBcompactCat-final) counting 84 sources, 30 of which are in common with ExtmapCat-final (Table 2). These make most of the ExtmapCat, with some of the excluded sources being the young sources without line emission described in the previous section. We deduce that PBcompactCat-final is a more complete version of ExtmapCat-final. The coordinates and best-fit properties of the clusters included in PBcompactCat-final are listed in Table 3. The distribution of PBcompactCat across the galaxy is shown in Figure 7.

All the sources with $E(B-V)>1.0$ mag are analyzed individually in Appendix B. For some of them, the best-fit $\chi^2_{\rm red}$ reaches a high value, above 50 (C203, C228, C233, C240, C274) suggesting inaccurate fit results. For two of the sources (C239 and C251), the photometry from the F657N filter was not used in the fit due to high uncertainty; nevertheless, its value suggests no Hα emission, in contrast with the NIR filters suggesting Paβ emission. Only three young and extincted sources, namely C213 (also included in the ExtmapCat-final sample under the ID number C10), C236, and C307, are good candidates for being retained in our final cut.

We show the resulting ages and extinctions from models with solar metallicity and with differential starburst extinction in Figure 12 (top panels). The overall trends discussed in Section 5.1.1 are recovered also in the PBcompactCat-final catalog, namely, solar-metallicity models predict older ages, while differential starburst extinction predicts younger ages and lower $E(B-V)$ values. The reference models remain the most viable also in this case, with the lowest median $\chi^2_{\rm red.}$ values (Figure 12, bottom panels).

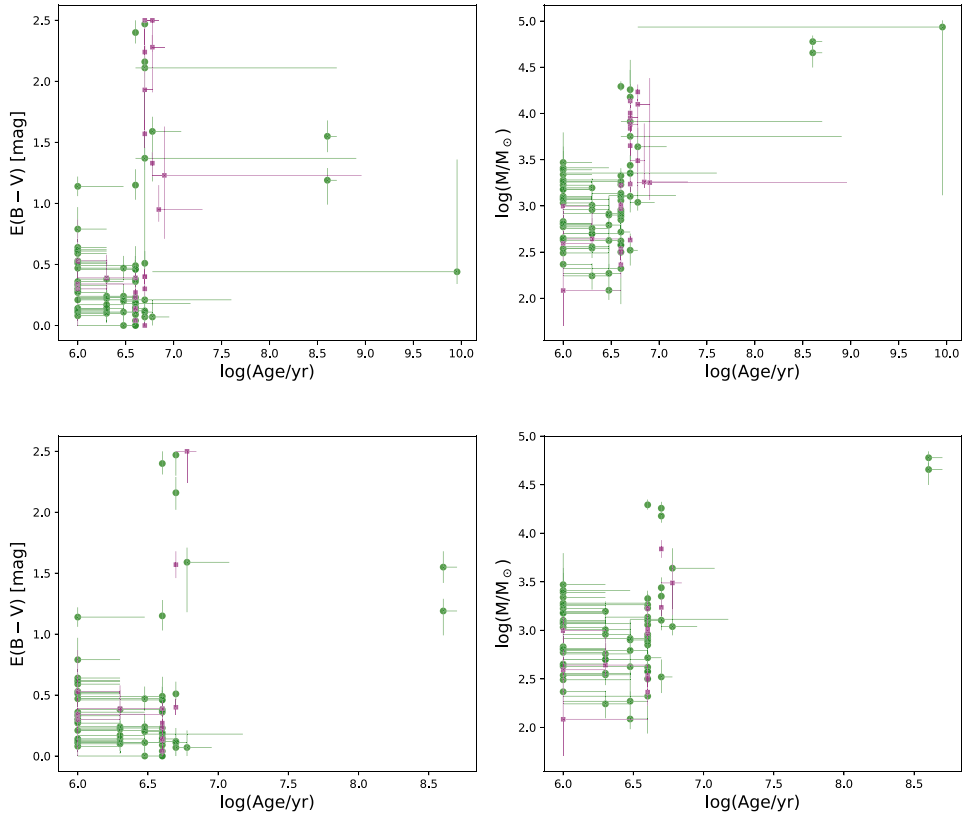

Figure 11. Same as Figure 8, but for the PBcompactCat sources. Blue has been changed into green, orange into magenta. The scale of the *X*-axis in the bottom-row plots was adapted to the narrower range spanned by the data in the final sample.

5.3. Sizes

The distributions of cluster sizes, derived in Section 4.2, are shown in Figure 13. The distributions have a median at $R_{\rm eff} = 1.28$ pc in the case of ExtmapCat-final and $R_{\rm eff} = 1.18$ pc in the case of PBcompactCat-final. These values are within the range $R_{\rm eff} \sim 0.5$–5 pc found in the Milky Way and in other nearby galaxies for clusters with masses around $10^3\,M_\odot$ (see, e.g., the review by Krumholz et al. 2019). While the size of clusters and their density is fundamental to determine their future evolution, the results found for our sample indicate that most of our sources are compact, possibly enough not to be affected by early gas loss, as suggested by Pfalzner & Kaczmarek (2013).

The sizes of stellar clusters in NGC 1313 were derived within the LEGUS collaboration; Ryon et al. (2017) obtained a median effective radius of 2.3 pc with a dispersion ± 1.2 pc. However, Ryon et al. (2017) limited the analysis to a complete subsample of the catalog at masses above $5000\,M_\odot$ and younger than 200 Myr. Only nine sources from our final catalogs reside in that range, while most of our sources have lower masses, making a detailed comparison impossible. In addition, the LEGUS catalog ignores sources with stellar-like PSF (see also Adamo et al. 2017), while our final catalogs contain some of such sources. Despite these differences, our values for the effective radii are consistent with the Ryon et al. (2017) results within their uncertainties, especially if we re-estimate our median values excluding unresolved sources for a more homogeneous comparison, finding $R_{\rm eff} = 1.62$ pc and $R_{\rm eff} = 1.58$ pc for ExtmapCat-final and PBcompactCat-final, respectively.

6. Discussion

6.1. Mass Estimates

We performed aperture photometry implementing an average aperture correction that assumes all clusters to be well described by Moffat light profiles with $R_{\rm eff} = 2.5$ pc. While the assumption is justified by studies of cluster sizes in NGC 1313 (Ryon et al. 2017), we discuss here whether using the individual size of each cluster in the photometric aperture correction would produce different mass estimates. We recall that different aperture corrections lead to different normalizations of the photometry and therefore affect only mass estimates, leaving the recovered ages and extinctions unchanged.

The procedure for deriving photometric results considering the individual sources' sizes was described in Section 4.2. We show in Figure 14 the distributions of masses for ExtmapCat-final and PBcompactCat-final derived with the two photometric analyses. The mass distribution derived via the aperture photometry analysis is peaked at a slightly larger median value for both catalogs. This is consistent with having found median effective radii of 1.28 and 1.18 pc for the ExtmapCat-final and PBcompactCat-final samples, respectively, which are smaller than the $R_{\rm eff} = 2.5$ pc used as reference for the average aperture correction. However, we note that the overall distributions are very similar, and we conclude that the mass distribution is not strongly affected by our choice of the average aperture correction.

We compare the median masses from our sample to the ones of the NGC 1313 LEGUS cluster sample. For this comparison, we select from the LEGUS catalogs only sources with ages $\leqslant 6$ Myr (the range covered by our final samples), and with visual class 1, 2,

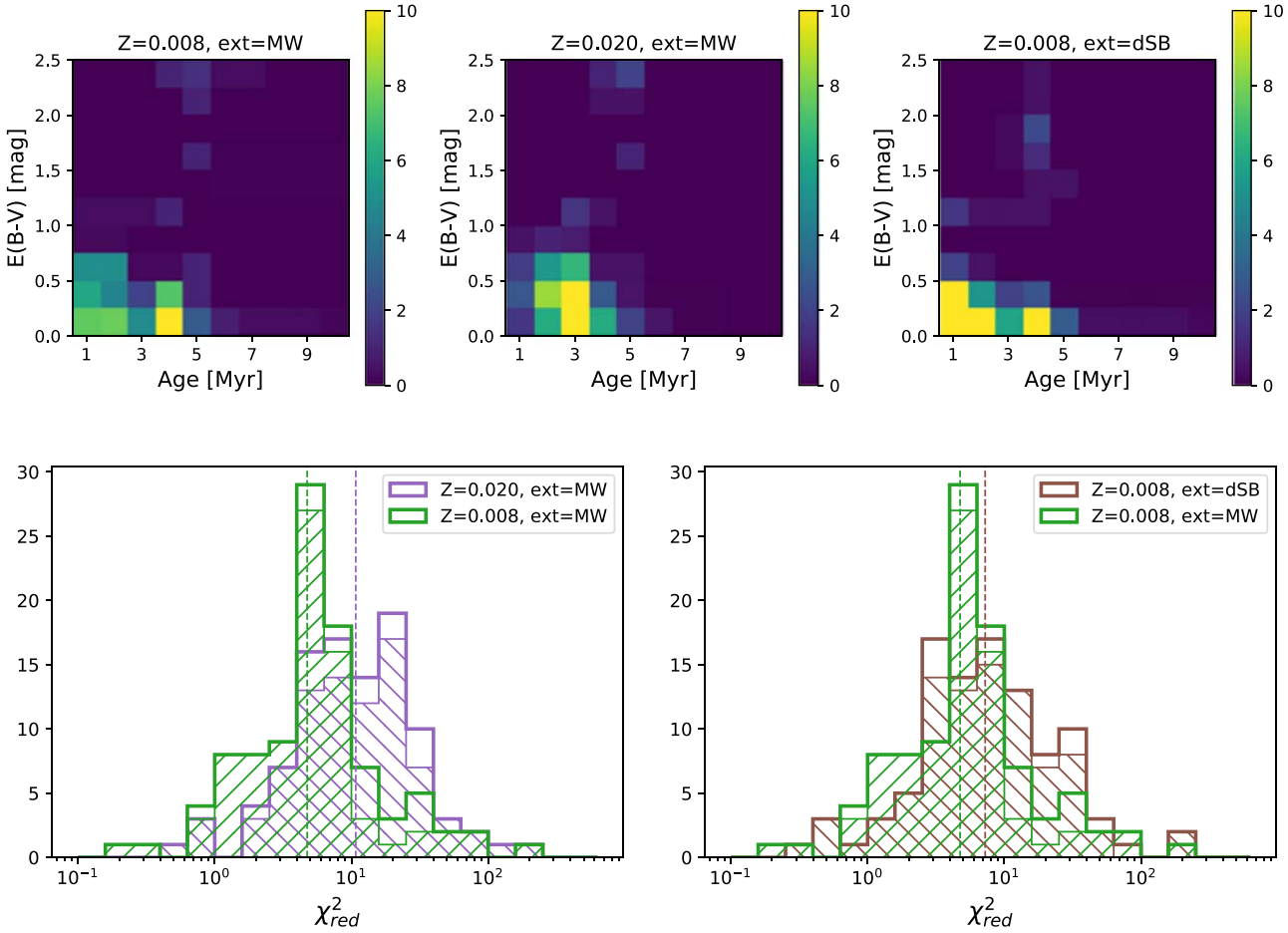

Figure 12. Same as Figure 8 (top panels) and as Figure 9 (bottom panels) for the PBcompactCat sample. The $\chi^2_{\rm red.}$ values are 4.7 for Milky Way extinction with $Z = 0.008$, 10.8 for $Z = 0.020$, and 7.2 for differential starburst extinction.

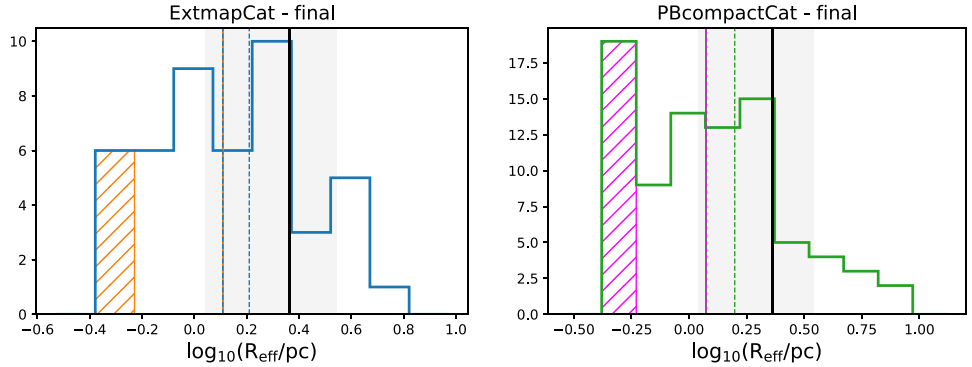

Figure 13. Distribution of sizes of the ExtmapCat-final (left) and PBcompactCat-final (right) samples. Sources with stellar-like PSF ($R_{\rm eff}$ <0.59 pc) have been highlighted using orange and magenta hatched histograms, and their sizes have been collapsed into a single bin. Both sources with stellar-like and with resolved profiles contribute to the measure of the median sizes, shown as vertical lines: blue-orange and green-magenta for the samples including sources with stellar-like profiles, dashed blue and dashed green excluding them. The black solid vertical lines indicate the median $R_{\rm eff}$ of the NGC 1313 clusters in the LEGUS sample, with the gray shaded area marking its uncertainty range, as reported by Ryon et al. (2017).

or 3, hence avoiding class 4 (that according to the LEGUS classification contains non-clusters, see Adamo et al. 2017). The median mass of the LEGUS sample, $M = 1256\,M_\odot$ is indicated in Figure 14 by a black vertical line. This value is identical to the median mass of our ExtmapCat-final sample when considering the aperture photometry analysis and is only slightly higher than the median mass of the PBcompactCat-final sample, $M = 935\,M_\odot$.

As mentioned in Section 5.1, the low cluster masses we are considering raise the problem of stochasticity, i.e., the stellar IMF of some of our clusters may not be fully sampled, as instead assumed by the models used for the SED fit (Section 4.3). On the other hand, we are considering clusters that power ionized gas, which need to host stars more massive than $8\,M_\odot$, therefore mitigating the stochasticity problem.

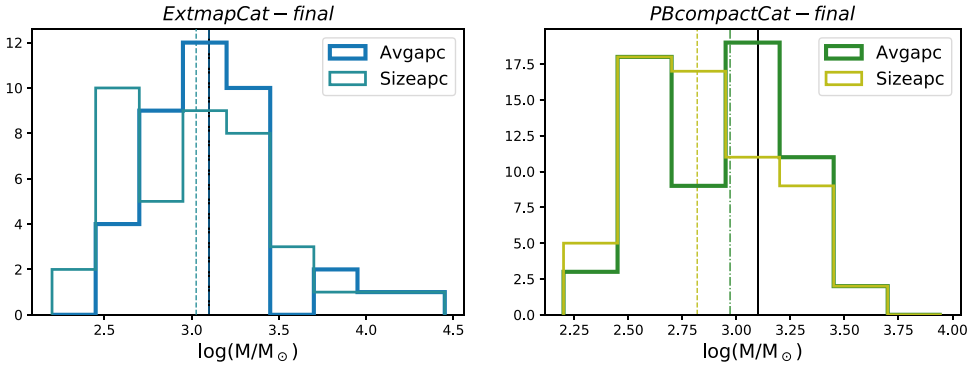

Figure 14. Mass distributions of the ExtmapCat-final sample (left panel) and PBcompactCat-final (right panel). Two distributions are shown for each catalog, one referring to photometry with average aperture correction (avgapc), the other referring to the size-photometry analysis (sizeapc). Vertical lines show their median distributions, and the black vertical line is the median mass of the NGC 1313 LEGUS sample in the age range 0–6 Myr.

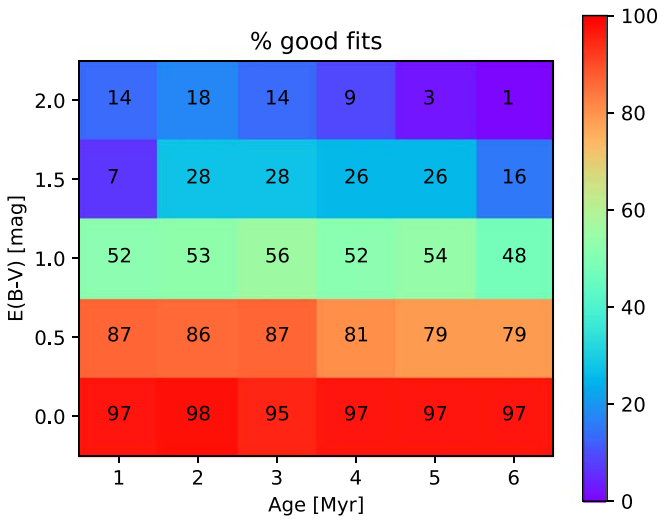

Figure 15. Percentage of sources with a retrieved good fit for all combinations of simulated ages and extinctions. We consider a source to have a good fit if its input age and extinction values fall into the uncertainty range given by the SED fitting process.

6.2. Are We Missing Sources?

6.2.1. Completeness of the Samples

Only a few young clusters from our final samples have extinctions $E(B-V)>1$ mag. The completeness test of Section 4.5 revealed that we expect less than 10% of sources with extinction up to $E(B-V)=1.5$ mag to be missed by our photometric analysis. We discuss now the possibility that the lack of sources with $E(B-V)>1$ mag can be due to imprecision in recovering properties from the SED fit.

We consider the simulated sources from the completeness test described in Section 4.5, and we collect the results of their SED fitting; in Figure 15, we build a matrix showing the fraction of retrieved sources with good fits. We consider good fits the cases where the original age and extinction are consistent with the derived values within the uncertainties. The matrix proves that we have completeness above 80% for sources with low extinction (up to 0.5 mag). The completeness decreases to ∼50% for $E(B-V)=1.0$ mag and to ∼25% for $E(B-V)=1.5$ mag. Typically a source can be detected up to an optical depth $\tau\sim1$, which in our case is reached for $E(B-V)\sim1.3$ mag at the wavelength of Paβ. Our findings are consistent with this expectation. In Figure 16, we plot all of the derived ages and masses using the method of Figures 8 and 12, in order to find if some combinations of ages and extinction are favored by the SED fitting procedure. The figure shows that, overall, ages around 5 Myr are favored by the fitting process compared to younger ages. On the other hand, in our data, we do not see many sources with age ∼4/5 Myr and extinctions of $E(B-V)\sim0.5/1.0$ mag; therefore, we have not over-predicted them.

Appendix C shows individual age–extinction density plots for each input age; for input ages of 4, 5, and 6 Myr, we recover consistent ages, while our fitting process cannot clearly distinguish ages of 1, 2, and 3 Myr. This limitation is related to models having very similar SEDs for such young ages.

As a final note, we remind readers that the approach used to extract our samples limit the detection to clusters that host stars massive enough to ionized hydrogen. As a consequence, we are practically blind to clusters that do not have massive stars.

6.2.2. Extincted Sources in Our Samples

From our analysis, we recover a total of 13 sources[16] whose best-fit properties fall in the ranges of ages ⩽6 Myr and $E(B-V)>1.0$ mag. Their best fits (distributions of $\chi^2_{\rm red.}$ values and photometry) are shown in Appendix B. We note that not all of the best-fit values can be considered robust, as suggested by the $\chi^2_{\rm red.}$ values, which in some cases is very high (>50). In particular, C10 and C307 are the two most robust cases, as their best fits follow the overall trend of the broadband SED and recover the line emission. For some other sources, the least-$\chi^2_{\rm red.}$ values are small, and therefore, we consider the fit reasonable, but the best-fit SEDs clearly miss reproducing the flux in one band: F547M in the case of C175–C236 (if starburst extinction is considered), F435W in the case of C251. All other cases are less robust either because of a limited number of filters with detections (e.g., C93–C272, C187–C239, C233) or because of large least-$\chi^2_{\rm red.}$ values (e.g., C142, C228, C274). We note that all those very extincted candidates are clearly displaced from the main distribution of extinctions, which extends up to $E(B-V)\sim1.0$ mag (see Figures 6 and 11). In addition, they all have ages between 4 and 6 Myr, while naively we would expect the most extincted sources to be the youngest.

[16] This total comes from considering both ExtmapCat-final and PBcompact-final samples and including also the best-fit values coming from the models with differential starburst extinction.

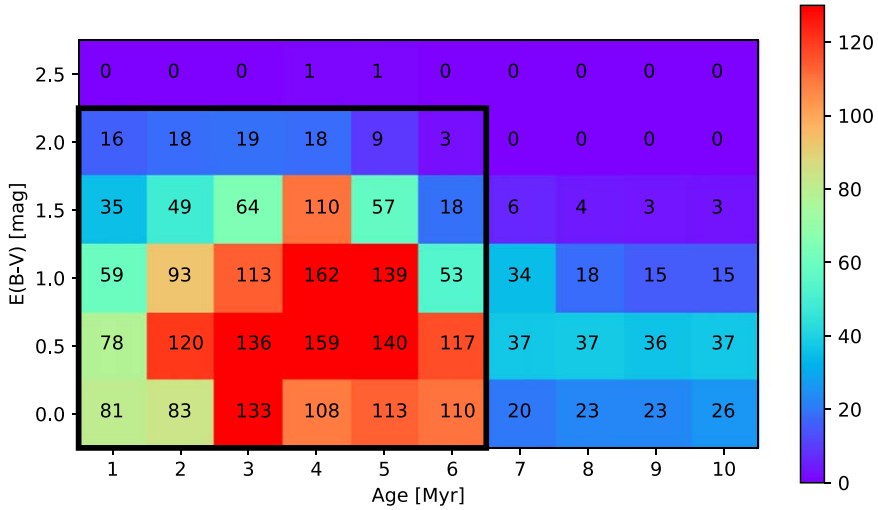

Figure 16. Density plots, as in Figures 8 and 12, for the sources, created for the completeness test. The input sources were simulated only in the age range [1; 6] Myr and $E(B-V)$ range [0.0; 2.0] mag, but a larger grid is plotted to account for uncertainties and fit results extending outside the initial grid (marked by a thick solid black contour). This plot indicates the ages and extinctions favored (or disfavored) by the fitting process.

As already pointed out in Section 5.1, they may be old clusters misinterpreted as younger and extincted ones due to age–extinction degeneracy in the SED fitting. Another hypothesis we cannot rule out is the random superposition (on the line of sight) of different epochs of star formation; the SED could be dominated by the oldest population and the line emission from a nearby younger embedded region. We kept all the discussed candidates in our final samples because the presence of line emission in all of them indicates they are young. However, we discuss in Section 6.3.1 how the properties of the sample would change when excluding them.

In both of our samples, a fraction of the sources were not fitted due to the lack of enough photometric detections. If those were young and very extincted clusters, we would be able to see their line emission, as the extinction has only a small impact on Hα and Paβ EWs (see Figure 4). As described in Section 5.1, we take into account in our analyses all sources with high-EW values, and we therefore took care not to leave out of the final samples possible young and extincted candidates.

The completeness analysis of Section 6.2.1 suggests that we should find approximately half of the $10^3\,M_\odot$ clusters with $E(B-V)\sim1$ mag, if they were there. We expect protoclusters to be deeply embedded into their natal cloud of gas and dust; such sources can only be seen through their MIR−FIR emission, and their investigation is beyond the scope of this study. However, we expect them to start forming massive stars and later to clear their cloud. Different concurrent factors may cause the absence of young sources with color excess in the range ∼1.0–2.5 mag. First of all, it could simply be the case that our data are not sufficiently deep for the observation of such sources. The completeness analysis just discussed, however, rules out this possibility, as even if there is incompleteness for high extinction, we still should be able to observe ∼half of the clusters with $E(B-V)\sim1.0$ mag. We remind readers that the comparison to the Spitzer 8 μm and to the CO emission maps revealed some compact regions missed by our extinction map and therefore by our source selection. Such regions could be associated with protostars/protoclusters. If this is the case, their study at high spatial resolution will be made possible by the advent of the James Webb Space Telescope.

Another possibility is that GMCs in NGC 1313 have low surface densities, and consequently, clusters form in relatively low-density environments. The extinction map derived in Section 3 (see Figure 1) indeed suggests that the most extincted regions of the nebular emission have $A_V\sim3.0$ mag, consistent with the high end of the color-excess main distributions at $E(B-V)\sim1.0$ mag derived in Section 5 (see Figures 6 and 11). An observed color excess $E(B-V)=1.0$ mag corresponds to a gas screen with a density of $150\,M_\odot\,\mathrm{pc}^{-2}$ (following the prescription by Bohlin et al. 1978 adjusting for subsolar metallicity); this estimate assumes a gas screen only between the source and the observer and constitutes therefore only a lower-limit estimate. ALMA observations indicate that CO clouds in NGC 1313 have surface densities ranging from ∼10 to $\sim300\,M_\odot\,\mathrm{pc}^{-2}$, with a median value of $\sim50\,M_\odot\,\mathrm{pc}^{-2}$ (a detailed description of the ALMA observation in NGC 1313 and its analysis will be presented in a coming paper, M. K. Finn et al. 2021, in preparation), consistent with the expectations estimated from the color excess and confirming the hypothesis of clusters form in relatively low-density environments.

Finally, the lack of embedded clusters could be due to (or enhanced by) an extremely short duration of the process of gas clearing due to feedback after the massive stars are formed (as suggested by e.g., Matthews et al. 2018; Hannon et al. 2019; Kruijssen et al. 2019; Chevance et al. 2020a). We discuss in the next section the typical timescales associated with the clearing of the natal gas cloud. We point out that in the case of nonuniform clouds and therefore in the presence of holes that give clear lines of sight into the cluster, the fit values will tend to show lower extinction. Such patchy clouds could still be the effect of stellar feedback since early times (see, e.g., Dale et al. 2014).

6.3. Typical Cluster Extinctions at Young Ages

6.3.1. Distribution of Extinctions

We consider in Figure 17 the distribution of extinctions, separating the samples in two age ranges, 1–3 and 4–6 Myr, to test for the presence of an age evolution. The median $E(B-V)$ values are 0.31 and 0.15 mag for ExtmapCat-final and 0.28 and 0.23 mag for PBcompactCat-final, for the age ranges 1–3 and 4–6 Myr, respectively. An age-dependent extinction is suggested for the first sample, with twice the color excess for the youngest age bin than the older age bin, while the second

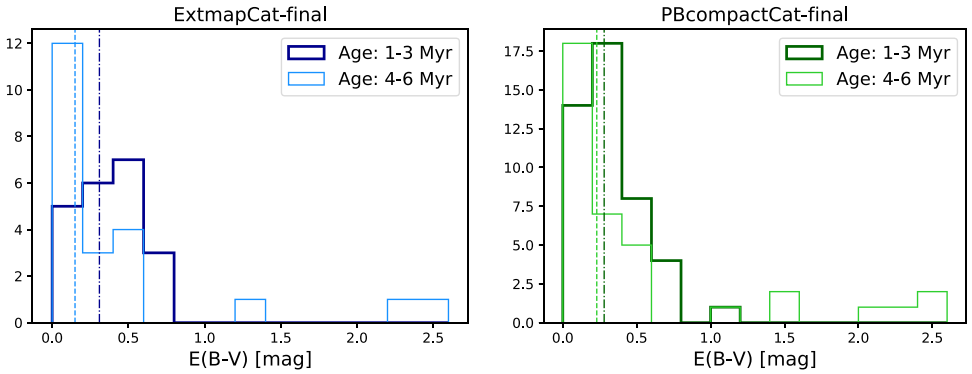

Figure 17. Distributions of extinctions for the ExtmapCat-final (left) and the PBcompactCat-final (right) samples. Dark colors refer to the age range 1–3 Myr, light colors for 4–6 Myr. The dotted–dashed and dashed vertical lines are the median values for the two age samples, respectively.

Table 4
Percentage of Clusters with $E(B-V)$ <0.25 mag, $F_{<0.25}$, in Two Age Ranges, 1–3 and 4–6 Myr

Sample	$F_{<0.25}$	
	1–3 Myr	4–6 Myr
ExtmapCat-final	41%	63%
PBcompactCat-final	45%	57%
LEGUS	84%	75%
LEGUS (in common)	25%	48%

Note. The last row reports the values of the sample in common between LEGUS and our final samples.

sample does not show a trend, but rather consistent values between the two age bins. We note that, despite having selected the sample to contain extincted clusters, half of our sources are consistent with having relatively low extinctions, $E(B-V)$ <0.25 mag, corresponding to $A_V \lesssim 0.75$ mag.

An alternative way of studying the typical extinctions of our samples is to consider the fraction of clusters below a certain limit. In Table 4, we report the fraction of clusters with $E(B-V)$ values below 0.25 mag, $F_{<0.25}$, i.e., the values of the lowest row in the density plot in Figures 8 and 12 divided by the total value in each column. These can be considered the fraction of low-extincted clusters. Once again, we separate the samples into two age bins.

The fractions varies from 41% to 63% for ExtmapCat-final and from 45% to 57% for PBcompactCat-final. As before, the ExtmapCat-final sample shows a slightly stronger age-dependent extinction trend than the other sample.

We can compare our samples to the cluster sample found by the LEGUS collaboration. We recall that the LEGUS sample selection is based on source detection in at least four filters in the NUV −optical range. The $E(B-V)$ values of LEGUS clusters with ages $\leqslant$6 Myr are shown in Figure 18 and the fraction of low-extinction clusters are collected in Table 4. Both the median values, 0.10 and 0.14 mag for the 1–3 and 4–6 Myr age ranges, respectively, and the fraction of low-extinction sources, 84% and 75% in the two age bins, respectively, indicate lower extinctions for the LEGUS clusters compared to our sample. This suggests, as expected, that the process of the sample selection in LEGUS is biased against clusters with higher extinctions.

There are 21 sources in common between the LEGUS and our samples. We consider their $E(B-V)$ distribution and fraction of low-extinction sources in Figure 18; their median $E(B-V)$ values (0.22 and 0.26 mag) are consistent with the values from the

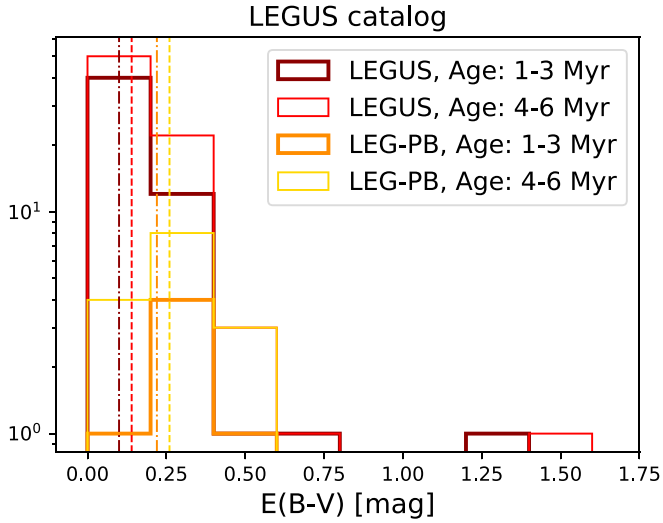

Figure 18. Distribution of extinction for the LEGUS sample in two age ranges, 1–3 and 4–6 Myr (dark red and red, respectively). The vertical dotted–dashed and dashed lines are the respective median values. The same distributions and medians for the subsample of sources in common with our samples (named here LEG-PB) are plotted with orange and yellow colors.

overall PBcompactCat-final sample. The same is true for the fraction of low-extinction clusters (see Table 4). We deduce that our samples are consistent with the higher-extinction portion of the LEGUS sample, i.e., we are biased (by construction) against clusters with low extinction. This is a direct consequence of the source selection method, which avoided regions with low extinction (in the extinction map derived in Section 3.1) and sources without a compact Paβ emission. Similarly, ∼80 clusters of our samples are not considered in LEGUS, and therefore, the latter sample is biased against sources with high extinction.

We create a "master" catalog by merging ExtmapCat-final, PBcompactCat-final, and the LEGUS catalog (removing the duplicates, i.e., the sources in common). The master catalog counts 254 sources, and we consider it as a more complete version of either our or the LEGUS samples; out of 208 sources with ages between 1 and 6 Myr in the "master" catalog, 76 (∼37%) are found exclusively in this study and were missed by LEGUS, while for 112 (∼54%), it is true for the opposite. In the case of the "master" catalog, we do not find an age evolution of the median $E(B-V)$ values, nor of $F_{<0.25}$ (Figure 19 and Table 5). As discussed in the previous section, most of the sources with $E(B-V)$ >1.5 mag are not robust results; repeating the analysis of the master catalog excluding

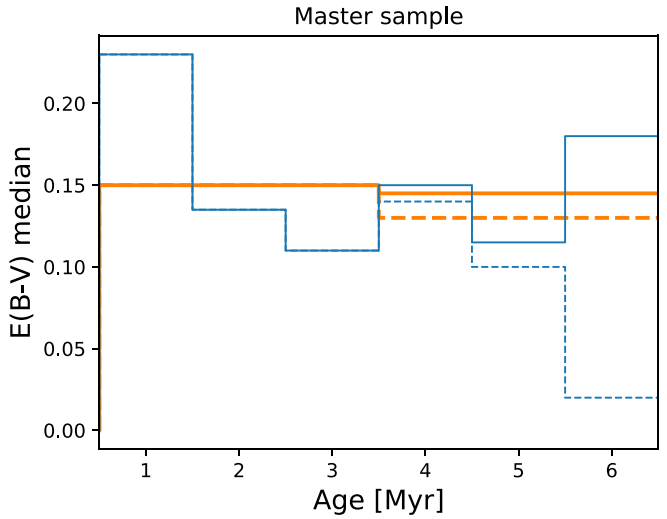

Figure 19. Median $E(B-V)$ as a function of ages for the master sample obtained by joining our final samples with the LEGUS one. The blue line considers an age division in bins of 1 Myr; the orange histogram divides the sample into two age bins (1–3 and 4–6 Myr). In both cases, we consider only sources with age $\leqslant$6 Myr. The dashed histograms exclude from the sample sources with $E(B-V)>1.5$, which, as discussed in the text, are not solid fits.

such sources yields an age trend of both the median and $F_{<0.25}$. In any case, we recover overall a low typical value for the cluster extinctions, with a median $E(B-V)\approx 0.15$ mag or lower. Similar low extinction values were recently confirmed also in the nearby galaxy NGC 4449 (Whitmore et al. 2020).

6.3.2. Hα and Paβ Morphology

Following the analysis of Hannon et al. (2019), we visually classify the morphology of the Hα and Paβ emission associated with each source in our samples. We follow their same classification scheme, mediated by Whitmore et al. (2011) and Hollyhead et al. (2015), who divide the sample into 3 classes:

1. concentrated, i.e., there is a compact H II region on the position of the cluster;
2. partially exposed, i.e., either the H II region shows a bubble-like morphology or only partially covers the cluster or emission is diffuse;
3. no emission, i.e., the target cluster is not associated with any nebular emission.

This division in classes is expected to reflect an evolution of the clusters, and indeed, both Hollyhead et al. (2015) and Hannon et al. (2019) found an increase in the median age of clusters when going from concentrated, to partially exposed, to no emission. We show, in Figure 20, age and extinction distributions of the clusters in our sample (merging together sources from ExtmapCat-final and from PBcompactCat-final), separating them into the three classes above. The classification was done independently in Hα and in Paβ, and therefore, we end up with two classifications for each cluster. For both line morphologies, we find a trend with age that have median values of 2, 4, and 6 Myr for "concentrated," "partially exposed," and "no emission" classes, respectively. We see a possible trend with extinction in the case of Paβ morphology, as median values decrease going from concentrated to no emission classes, but the same is not true in the case of Hα morphology. In the latter case, the median extinction of the "no emission" class is driven by the group of clusters with high extinctions.

Table 5
Percentage of Clusters with $E(B-V)<0.25$ mag, $F_{<0.25}$, for the Master Catalog, i.e., the Merged Catalog of Our Own Catalogs with the LEGUS One (See Text), Both in Age Bins of 1 Myr and in the Two Age Ranges 1–3 and 4–6 Myr

Age	$F_{<0.25}$	w/o high $E(B-V)$
1 Myr	64%	64%
2 Myr	67%	67%
3 Myr	81%	81%
4 Myr	71%	73%
5 Myr	73%	84%
6 Myr	68%	87%
1–3 Myr	70%	70%
4–6 Myr	71%	77%

Note. The second column reports $F_{<0.25}$, excluding from the sample the sources with $E(B-V)>1.5$ mag.

An interesting feature coming out of the plots in Figure 20 is that the almost totality of clusters with $E(B-V)>1.5$ have compact Paβ emission but no Hα. If we assume their extinction values are correct, we expect the absence of Hα emission to be driven by the elevated extinction. We test this hypothesis by deriving, from the Paβ line emission map (Section 3.1), the Paβ flux of those seven sources and converting it into an expected Hα flux (taking into account the extinction of each source). The derived Hα fluxes span the range (2–25) $\times 10^{-20}$ erg cm^{-2} Å^{-1}. Assuming their flux is uniformly distributed over a circular region of 1 pc radius (1.17 px at the distance of NGC 1313), their surface brightness is between 1σ and 14σ above the noise at their coordinates. Four out of seven of them have an expected Hα emission more than 3σ above the detection limit. The hypothesis is therefore only partially confirmed. We also note that all seven sources considered are found in regions far from the large star-forming subregions (see Figure 7) and appear in the Paβ map as isolated sources.

Assuming to have a complete catalog of clusters covering the age range 0–10 Myr, Hannon et al. (2019) estimate the timescale associated with each of the Hα morphological classes by simply converting the fraction of sources in the class to a timescale in Myr. We discussed in the previous section how the LEGUS catalog that the authors used for this estimate is incomplete, being biased against extincted sources. We repeat their analysis using the master catalog created by merging our final samples with the LEGUS catalog. We report in Table 6 the timescales for each morphological stage for the LEGUS sample (of NGC 1313 only, while Hannon et al. 2019 reported the value calculated considering together three of the LEGUS galaxies), for our final samples alone, and for the merged sample. In the case of our samples alone, we assume that they are representative of the age range 0–6 Myr, while for the other two samples we consider an age range of 0–10 Myr. The addition of our samples to the LEGUS one prolongs the timescale of the "concentrated" stage from ∼2 Myr to ∼3 Myr, while the intermediate stage of partial emission remains ∼1.5–2.0 Myr long. We conclude that already at ∼3 Myr, the H II regions typically begin to disperse, and by ∼5 Myr, there is very little or no nebular emission left around the clusters in NGC 1313.

7. Summary and Conclusions

Using NUV–optical–NIR HST broad- and narrowband observations of the nearby galaxy NGC 1313, we looked for

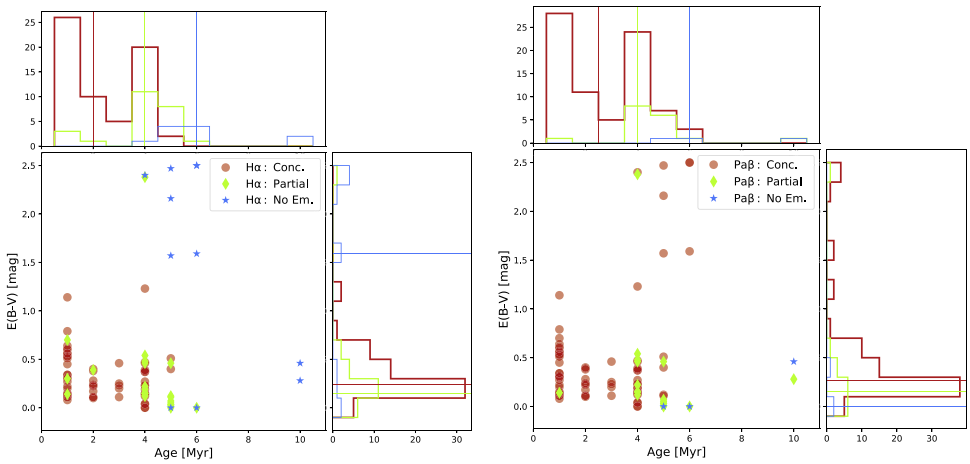

Figure 20. Distributions of ages and extinction for our final samples (merged together), color-coding the clusters based on their Hα morphology (left) and Paβ morphology (right). Horizontal and vertical solid lines in the side histograms refer to the median values of each morphological class. The few sources that lack both Hα and Paβ emission were included in the ExtmapCat because they are located in regions with diffuse nebular emission or very close to regions with elevated nebular emission.

Table 6
Relative Fractions and Inferred Timescale of Each Hα Morphological Class for the Sample of Hannon et al. (2019; Considering Only the Clusters of NGC 1313), Our Final Samples, and a Master Catalog Merging Them

Sample	Age Range					
	Concentrated		Partial Emission		No Emission	
Hannon et al. (2019)	19.1%	1.9 Myr	16.3%	1.6 Myr	64.6%	6.5 Myr
This work	65.6%	3.9 Myr	25.0%	1.5 Myr	9.4%	0.6 Myr
Merged	30.6%	3.1 Myr	18.4%	1.8 Myr	51.0%	5.1 Myr

Note. The timescales for our samples alone have been considered over a total timescale of 6 Myr, and because of that, the "no emission" stage lasts only 0.6 Myr.

young and embedded star clusters. In particular, new NIR data are used to derive a map of the Paschen-β nebular emission and to characterize extincted sources possibly missed by previous analysis focused on the NUV–optical part of the spectrum.

We extract a catalog of possible candidates in two different ways:

1. the first selection is made by using a map of nebular extinction derived from Hα and Paβ observations. Subregions of the galaxy where the extinction is higher than $A_V \geqslant 0.8$ mag were searched for sources in the F814W filter with counterparts in the NIR filters;
2. with a complementary approach, we select sources with compact Paβ emission within the entire galaxy.

The sources in the two resulting catalogs, named ExtmapCat and PBcompactCat, respectively, are analyzed photometrically and via a least-χ^2 broad- and narrowband SED fit, in order to derive their ages, masses, and extinctions. The effective radius of each source is estimated assuming a spherical symmetrical Moffat profile; most of the sources in the initial catalogs have a light profile consistent with stars. Among the star-like sources, only the ones with Hα and Paβ EWs higher than 317 Å and 95 Å, respectively, i.e., consistent with being younger than 6 Myr according to our models (see Section 4.4), are retained in the final samples. In addition, only sources with small uncertainties in the derived ages are considered in the final samples.

The final samples count 46 and 84 sources for ExtmapCat-final and PBcompactCat-final, respectively. Thirty clusters are in common between the two final catalogs. The median size of the sources in the final samples is $R_{\rm eff} \approx 1$ pc (Figure 13). Overall, they are mainly distributed in the age range 0–6 Myr, with extinctions $E(B-V) \leqslant 1.0$ mag and masses in the range $\log_{10}(M/M_\odot) = 2.5$–$3.5$ (Figures 6 and 11). The ages derived via the broadband SED fit are consistent with the ages that would be estimated from the Hα and Paβ equivalent widths values (Figures 5 and 10). A comparison between models with various metallicities and extinction curves reveals that clusters in NGC 1313 are better fit by models with subsolar metallicity, $Z = 0.008$, and Milky Way extinction curve (Figures 9 and 12 and, and Appendix B).

In addition, to use the results from photometry and SED fitting, we classify the morphology of the Hα and Paβ emission associated with each of the sources in the final samples; following the example of previous studies (e.g., Whitmore et al. 2011; Hollyhead et al. 2015; Hannon et al. 2019), we used a three-class division, namely "concentrated" nebular emission, "partially exposed," and sources with "no (nebular) emission" associated. The classes are assumed to describe the time evolution of the gas from a dense cloud to the dispersion. Most of the sources in our final samples fall into the first class, especially for what concerns the Paβ emission; we remind readers that the PBcompactCat sample is expected to contain sources with concentrated Paβ emission by construction.

Despite the majority of the sources in the final catalogs having low extinctions, for 13 sources, we derived $E(B-V) > 1.0$ mag. Not all of their fits are robust; in some cases, the $\chi^2_{\rm red.}$ associated with the best fit are high (>50); in some other cases, we have detections only in a few ($\sim$5) filters. Several of these sources have concentrated Paβ emission but no Hα detected (Figure 20); based on their Paβ flux and their derived $E(B-V)$ values, more than half of them should have Hα detectable. In addition, they are located far from the main star-forming regions (Figure 7). Overall, we consider them only as possible candidates for young and extincted regions. Only two of them (with $E(B-V)$ slightly above 1.0 mag) have robust fits.

We expect the young clusters to form in dense clouds of gas and dust and to be still embedded in their natal cloud at birth.

We propose a few hypotheses for the small number of young and extincted sources observed.

1. Low surface densities of the GMCs hosting star formation. An extinction of $E(B-V)=1.0$ mag would correspond to a gas screen with a surface density of $150\,M_{\odot}\,\mathrm{pc}^{-2}$, consistent with the average values for GMCs in NGC 1313 as revealed by ALMA observations.
2. An extremely short timescale for the clearing of the natal cloud due to feedback, on the order of ∼1 Myr; short timescales could be related to the low gas surface density discussed in the previous point.
3. Via a completeness test, we estimate an incompleteness of ∼50% at $E(B-V)=1.0$ mag (see Figure 15). According to this test, we would expect to recover ∼25% of the sources with $E(B-V)$ between 1.0 and 2.0 mag, but we found only one source in such extinction range and with age ⩽3 Myr (out of 45 total sources with age ⩽3 Myr found).

We study the distribution of extinction as a function of cluster ages, expecting younger sources to be more extincted.

1. We recover a weak dependence of $E(B-V)$ with age (Figure 17); ∼40% of the sources with ages in the range 1–3 Myr have $E(B-V)<0.25$ mag, while the percentage rises to ∼60% for the sources with ages 4–6 Myr. These data confirm that a significant fraction of sources have low extinction already at ages ⩽3 Myr.
2. A clear trend is observed between the morphology of the Paβ emission and the age and extinction of the relative cluster; sources with concentrated emission are on average younger and more extincted than sources with partial or no emission (Figure 6).

We include the clusters from the LEGUS catalog (focused on NUV–optical sources, while our catalogs are focused on optical–NIR) to create a "master" catalog, more representative of the entire young cluster population of NGC 1313.

1. Repeating the study of the extinctions on the master catalog, we find weak or no evolution with age, depending on whether the sources with $E(B-V)>1.5$ mag discussed above are excluded from consideration or not (Figure 19). At best, 70% of the clusters with ages ⩽3 Myr have low extinctions (below $E(B-V)<0.25$), with the percentage rising to 77% in the age range 4–6 Myr.
2. Assuming that the "master" sample is representative of the NGC 1313 cluster population in the age range 0–10 Myr, we use the fraction of sources in each class to estimate its typical timescale. We recover 3.1 Myr for the concentrated phase, 1.8 Myr for the "partial emission," and 5.1 Myr for the "no emission" phase. This result prolongs the expected timescale for clearing the cloud by 1 Myr (∼50%) compared to a previous estimate based only on NUV–optical data.

Clusters in NGC 1313 appear to have cleared the gas cloud around them by the time they reach an age of 5 Myr, and many of them are already almost gas free within the first 3 Myr. We conclude that the inclusion of a tracer more transparent to extinction (NIR observations) has allowed the fraction of clusters that are missed in optical–NUV studies to be recovered and to better pin down previous estimates of the duration of the embedded phase to 3 Myr; including young embedded clusters in NGC 1313 changes previous estimates of the short feedback timescales from clusters by ∼50% (from ∼2 Myr to ∼3 Myr), bringing it closer to the timescales for the first supernova explosions, which could occur as early as ∼4 Myr (e.g., Sukhbold et al. 2016). In addition, photoionization, radiation pressure, and winds can open channels before supernovae explode for low-mass GMCs ($\sim10^4$–$10^5\,M_{\odot}$, e.g., Dale et al. 2014; Dale 2015).

The analysis also suggested that the median age of the cluster correlates better with the morphology of the nebular emission (Figure 20) than with the cluster extinction (Figures 17 and 19); we deduce that the Hα (and Paβ) morphology is a good tracer of the cluster age evolution. On the other hand, median cluster extinctions also show some correlation with the ionized gas morphology (Figure 20), but also reveal that many clusters with "concentrated" nebular emission associated are not very extincted, with $E(B-V)$ ∼0.25 mag, i.e., even when a cluster is still surrounded by a compact gas cloud, its effect on the cluster extinction can be low. We speculate that this could be caused by nonuniform gas-dust clouds, where holes in the line-of-sight direction allow the escape of stellar radiation.

We point out that the current study considers only clusters in NGC 1313, a single galaxy with a given metallicity (best estimate: $Z=0.008$) and SFR density ($\Sigma_{\mathrm{SFR}}\sim0.01\,M_{\odot}\,\mathrm{yr}^{-1}\,\mathrm{kpc}^{-2}$). In addition, most of the cluster masses in NGC 1313 are distributed around a mass of $\sim10^3\,M_{\odot}$. We plan in the near future to extend this study to galaxies with different properties and clusters with a wider range of masses in order to estimate if and how the interaction between the very young clusters and their cloud is affected by the host galaxy properties and by the properties of cluster themselves.

Based on observations made with the NASA/ESA Hubble Space Telescope, obtained at the Space Telescope Science Institute, which is operated by the Association of Universities for Research in Astronomy, Inc., under NASA contract NAS 5-26555. These observations are associated with program # 15330. Support for program # 15330 was provided by NASA through a grant from the Space Telescope Science Institute. M.M. and D.C. acknowledge partial support from this grant. V.B. acknowledges support from the same grant. K.E.J. acknowledges support from NSF grants 1413231 and 1716335. A.A. acknowledges the support of the Swedish Research Council, Vetenskapsrådet, and the Swedish National Space Agency (SNSA). We appreciated the useful comments of the anonymous referee.

Facility: HST.

Appendix A
Further Details of the Size Analysis

In Section 4.2 we measure the size of clusters using a size-photometry routine; at the same time, this routine allows to measure the cluster fluxes taking into account the width of their light profile, without relying on an aperture correction. In each filter, the source is modeled as a convolution between the instrumental PSF K_f, where f denotes the current filter, and a Moffat profile (Elson et al. 1987). In order to take a nonuniform sky background into account, the source model was added to a first-degree polynomial (described by three parameters, c_0, c_x, and c_y). The observable model (M) is therefore parameterized

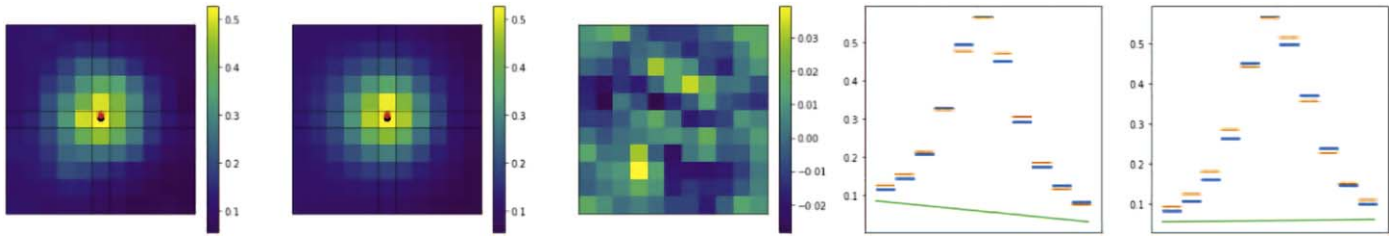

Figure A1. Example of a source whose size and photometry are fitted with the size-photometry approach. From left to right are shown a 2D cutout of the data in F814W (in count s^{-1}), its 2D best-estimated model, the 2D residuals, and the 1D profiles (central row and column) showing data in blue, and the best model of the source in orange and the best model of the background in green.

as

$$M_f(x, y|x_0, y_0, F, r_c, c_0, c_x, c_y) = [K_f{*}(F/F_0 \cdot (1 + (r/r_c)^2)^{-1.5})] + c_0 + c_x x + c_y y, \quad \text{(A1)}$$

where r_c is related to the effective radius by $R_{\rm eff} = \sqrt{3}\, r_c$ and the radial distance r is defined as $r = \sqrt{(x - x_0)^2 + (y - y_0)^2}$, where x, y are the pixel coordinates and x_0, y_0 are the source coordinates. F and r_c parameterize the flux and size of the source, respectively. We point out that the PSF profile K_f is normalized and that the Moffat profile is also normalized via F_0. Because nearby sources can cause contamination especially in the bluer filters, we use F814W to estimate the coordinates and the size of each of the sources. Figure A1 shows an example from the fit of one of the clusters. The flux uncertainties are correlated with uncertainties on the other parameters, especially with the size. In order to take it into account, we repeat the fit in the F814W filter twice, the second time keeping fixed the coordinates and size. We consider for each source the relative uncertainty given by the size and position uncertainties:

$$R_{r_c xy} = \frac{\sqrt{F^2_{\rm F814W,err,1} - F^2_{\rm F814W,err,2}}}{F}, \quad \text{(A2)}$$

where $F_{\rm F814W,err,1}$ and $F_{\rm F814W,err,1}$ are the total uncertainties on the flux uncertainties in the two repetitions of the fit. Then, for every filter f, we use this relative value to correct the uncertainty derived from the fit with fixed size, $F_{f,\rm err}$:

$$F_{f,\rm err,tot} = \sqrt{(R_{r_c xy} \cdot F_f)^2 + (F_{f,\rm err})^2}, \quad \text{(A3)}$$

where F_f is the flux measured for the current source in the filter f.

Appendix B
Individual Fit Results

We report in this section the plots of the SED fitting process for some of the sources discussed in the main text.

B.1. Comparing Solar and Subsolar Metallicities

We show in Figure B1 some examples of the observed broadband SED of young sources with line emission and the best-fit SED values using solar and subsolar metallicities. While in both cases the best-fit values for the ages denote young sources (age $\leqslant$5 Myr), the models with subsolar metallicity are more capable of capturing the flux difference observed between the F555W and the F547M filters. Also, the values of the best $\chi^2_{\rm red}$ in the two cases confirm this trend.

B.2. Young and Extincted Candidates

We show in Figures B2 and B3 the sources whose best-fit results suggest them being young and extincted. The single cases are discussed in Section 6.2.2.

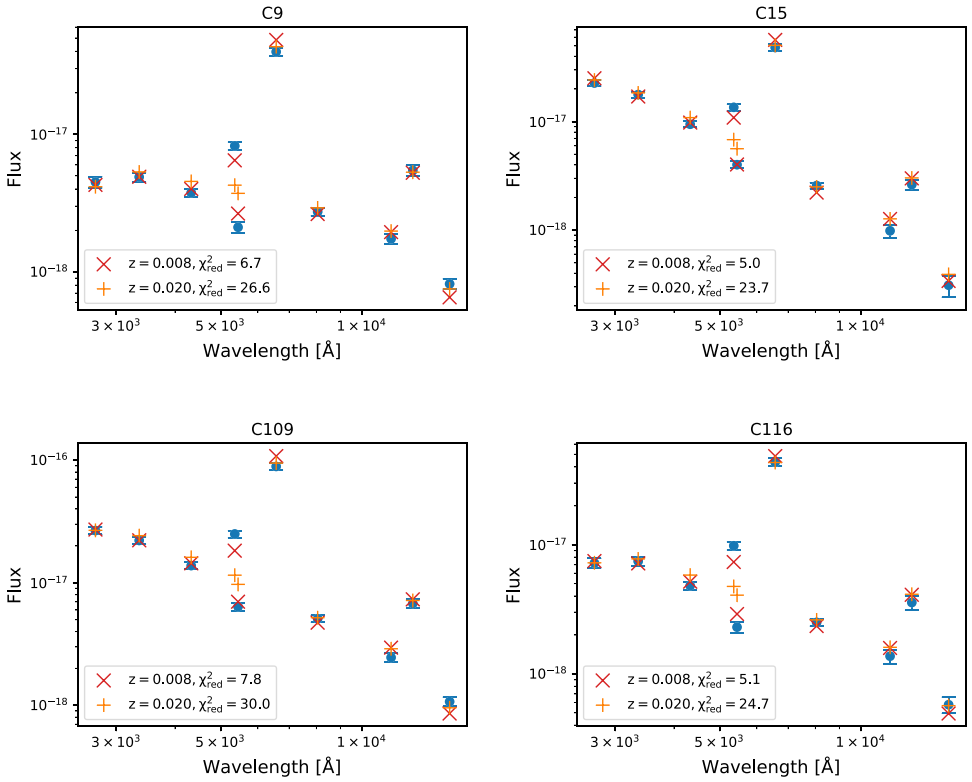

Figure B1. Examples of fits of young clusters using models with different metallicities, $Z = 0.008$ (red crosses) and $Z = 0.020$ (orange plus). Data and photometric uncertainties are shown as blue circles and relative error bars. Filters F547M and F555W determine the main difference in the recovered $\chi^2_{\rm red.}$ values, suggesting that models with subsolar metallicities are a better assumption for the young clusters in NGC 1313.

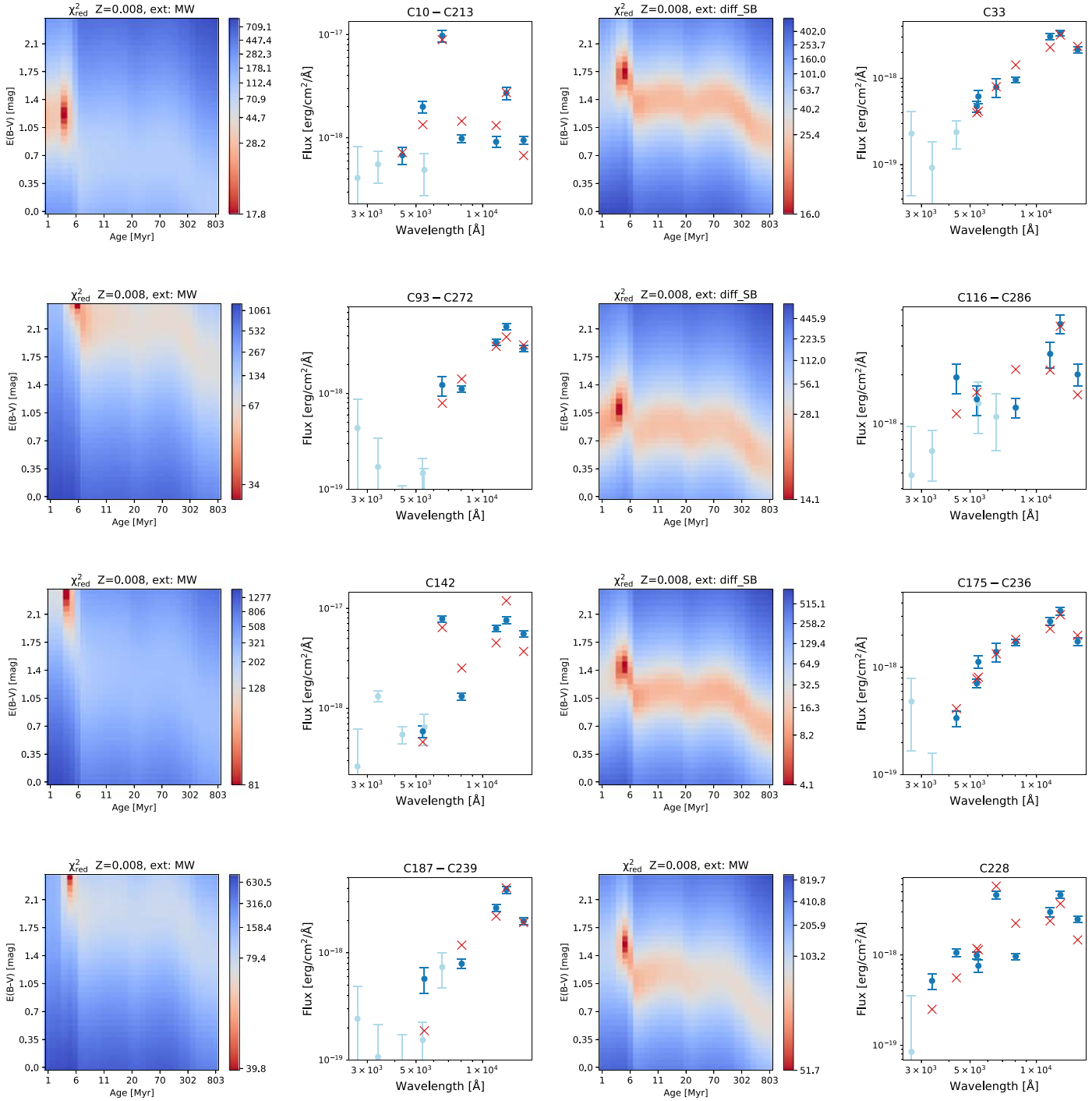

Figure B2. Candidate young and extincted sources from both the ExtmapCat-final and PBcompactCat-final samples. For each source, we show the distributions of $\chi^2_{\rm red.}$ values on the age–extinction grid used in the fit process (cut at ages ∼1 Gyr) and the fluxes from the best-fit (red crosses) plotted over the photometric data (blue circles). The data not used in the fit because of either large uncertainty or contamination are plotted with shaded blue color.

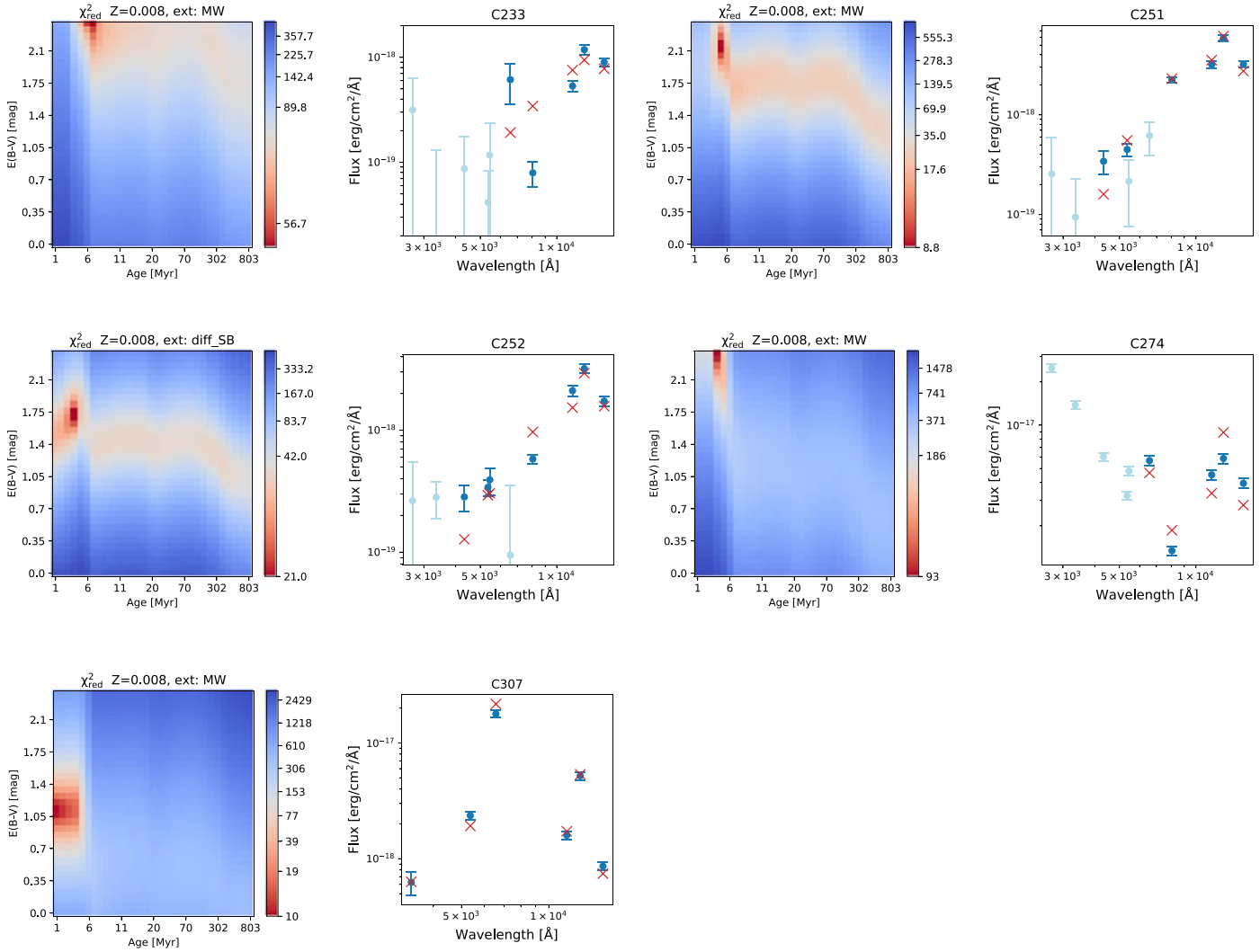

Figure B3. Continuation of Figure 2.

Appendix C
Additional Plots for the Completeness Test

We report in Table C1 and Figure C1 a summary of the completeness in detecting photometrically the input sources in the context of the completeness test described in the main text in Sections 4.5 and 6.2.1. In Figure C2, we report the density plot showing how the recovered ages and extinctions are distributed, for each of the input ages used. The main conclusion that can be drawn from Figure C2 is that our age determination via broadband (and narrowband) SED fitting is degenerate for very young ages; in fact, for the simulated clusters with age of 1 Myr, we retrieved estimated ages equally split between 1 and 2 Myr. Similarly, the estimated ages for the simulated clusters of 2 Myr span the entire range up to 3 Myr with almost constant frequency. Only for simulated clusters with ages of 4 Myr (and older) does the SED fitting return consistent ages, with little age spread. This effect is mainly caused by the stellar models used being very similar with each other for young ages, causing degeneracy in the SED fitting process. For this reason, in the main text, we consider as degenerate the SEDs with ages of 3 Myr and below.

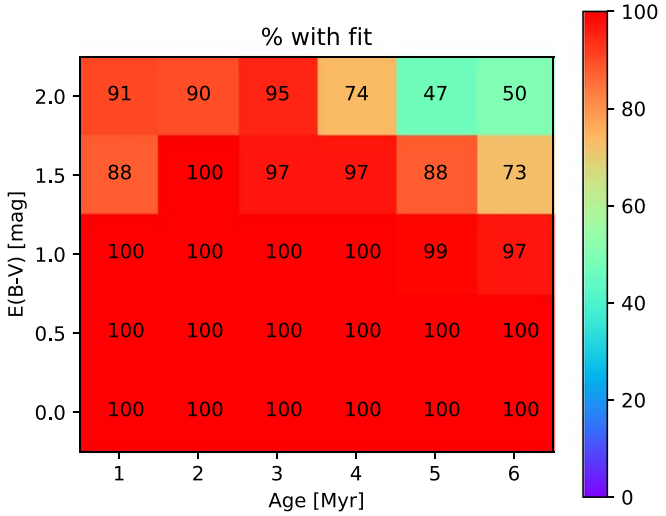

Figure C1. Percentage of simulated clusters with detections in at least five filters (counting both broad and narrow ones). This is the minimum number of filters required for the fit.

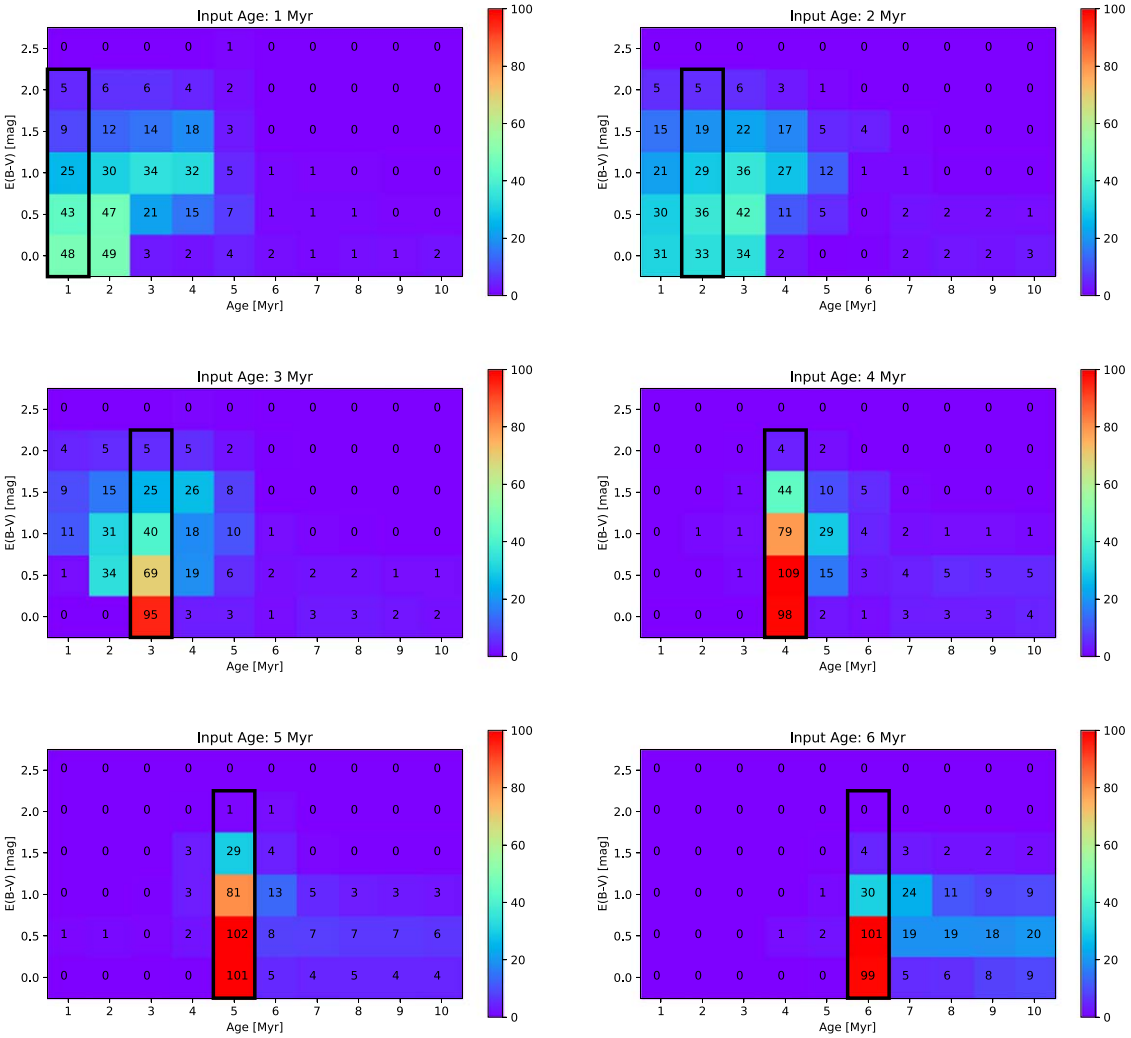

Figure C2. Density plot of the recovered ages and extinctions, as in Figure 16, but separating the input sources per age bins (as indicated by the black thick contours).

Table C1
Number of Simulated Sources with Photometry Recovered with an Uncertainty below 0.3 mag (i.e., S/N >3) for Each Combination of Age and Extinction (out of an Initial Value of 100)

Age	$E(B-V)$ F814W					$E(B-V)$ F128N				
	0.0	0.5	1.0	1.5	2.0	0.0	0.5	1.0	1.5	2.0
1 Myr	100	100	99	95	86	99	98	99	99	98
2 Myr	100	100	99	97	80	100	100	99	100	96
3 Myr	100	99	100	92	85	100	99	99	93	93
4 Myr	100	99	100	94	84	99	97	98	90	86
5 Myr	100	99	100	95	75	98	97	90	92	73
6 Myr	100	100	100	97	90	97	97	96	85	82

Note. Values are reported for two pivotal filters in the catalog extraction, F814W (for ExtmapCat) and F128N (for PBcompactCat).

ORCID iDs

Matteo Messa https://orcid.org/0000-0003-1427-2456
Daniela Calzetti https://orcid.org/0000-0002-5189-8004
Angela Adamo https://orcid.org/0000-0002-8192-8091
Kathryn Grasha https://orcid.org/0000-0002-3247-5321
Kelsey E. Johnson https://orcid.org/0000-0001-8348-2671
Elena Sabbi https://orcid.org/0000-0003-2954-7643
Linda J. Smith https://orcid.org/0000-0002-0806-168X
Molly K. Finn https://orcid.org/0000-0001-9338-2594
Zesen Lin https://orcid.org/0000-0001-8078-3428

References

Adamo, A., Kruijssen, J. M. D., Bastian, N., Silva-Villa, E., & Ryon, J. 2015, MNRAS, 452, 246
Adamo, A., Ryon, J. E., Messa, M., et al. 2017, ApJ, 841, 131
Adamo, A., Zackrisson, E., Östlin, G., & Hayes, M. 2010, ApJ, 725, 1620
Aversa, A. G., Johnson, K. E., Brogan, C. L., Goss, W. M., & Pisano, D. J. 2011, AJ, 141, 125
Bastian, N., Adamo, A., Gieles, M., et al. 2012, MNRAS, 419, 2606
Bastian, N., Schweizer, F., Goudfrooij, P., Larsen, S. S., & Kissler-Patig, M. 2013, MNRAS, 431, 1252
Bohlin, R. C., Savage, B. D., & Drake, J. F. 1978, ApJ, 224, 132
Calzetti, D., Armus, L., Bohlin, R. C., et al. 2000, ApJ, 533, 682
Calzetti, D., Johnson, K. E., Adamo, A., et al. 2015a, ApJ, 811, 75
Calzetti, D., Lee, J. C., Sabbi, E., et al. 2015b, AJ, 149, 51
Cardelli, J. A., Clayton, G. C., & Mathis, J. S. 1989, ApJ, 345, 245
Chandar, R., Fall, S. M., & Whitmore, B. C. 2015, ApJ, 810, 1
Chevance, M., Kruijssen, J. M. D., Hygate, A. P. S., et al. 2020a, MNRAS, 493, 2872
Chevance, M., Kruijssen, J. M. D., Vazquez-Semadeni, E., et al. 2020b, SSRv, 216, 50
Corbelli, E., Braine, J., Bandiera, R., et al. 2017, A&A, 601, A146
Dale, J. E. 2015, NewAR, 68, 1
Dale, J. E., Ngoumou, J., Ercolano, B., & Bonnell, I. A. 2014, MNRAS, 442, 694
de Vaucouleurs, G. 1963, ApJ, 137, 720

Elmegreen, B. G., & Elmegreen, D. M. 2019, ApJS, 245, 14
Elmegreen, B. G., & Elmegreen, D. M. 2020, ApJ, 895, 71
Elmegreen, B. G., Elmegreen, D. M., & Efremov, Y. N. 2018, ApJ, 863, 59
Elson, R. A. W., Fall, S. M., & Freeman, K. C. 1987, ApJ, 323, 54
Ferland, G. J., Porter, R. L., van Hoof, P. A. M., et al. 2013, RMxAA, 49, 137
Finn, M. K., Johnson, K. E., Brogan, C. L., et al. 2019, ApJ, 874, 120
Fitzpatrick, E. L. 1999, PASP, 111, 63
Gaia Collaboration, Brown, A. G. A., Vallenari, A., et al. 2018, A&A, 616, A1
Grasha, K., Calzetti, D., Adamo, A., et al. 2017a, ApJ, 840, 113
Grasha, K., Calzetti, D., Adamo, A., et al. 2019, MNRAS, 483, 4707
Grasha, K., Calzetti, D., Bittle, L., et al. 2018, MNRAS, 481, 1016
Grasha, K., Elmegreen, B. G., Calzetti, D., et al. 2017b, ApJ, 842, 25
Hannon, S., Lee, J. C., Whitmore, B. C., et al. 2019, MNRAS, 490, 4648
Hollyhead, K., Bastian, N., Adamo, A., et al. 2015, MNRAS, 449, 1106
Jacobs, B. A., Rizzi, L., Tully, R. B., et al. 2009, AJ, 138, 332
Johnson, K. E., Brogan, C. L., Indebetouw, R., et al. 2018, ApJ, 853, 125
Johnson, K. E., Hunt, L. K., & Reines, A. E. 2009, AJ, 137, 3788
Johnson, K. E., Indebetouw, R., Watson, C., & Kobulnicky, H. A. 2004, AJ, 128, 610
Johnson, K. E., & Kobulnicky, H. A. 2003, ApJ, 597, 923
Johnson, K. E., Kobulnicky, H. A., Massey, P., & Conti, P. S. 2001, ApJ, 559, 864
Johnson, K. E., Leroy, A. K., Indebetouw, R., et al. 2015, ApJ, 806, 35
Johnson, L. C., Seth, A. C., Dalcanton, J. J., et al. 2016, ApJ, 827, 33
Kennicutt, R. C., Jr., Lee, J. C., Funes, J. G., et al. 2008, ApJS, 178, 247
Kepley, A. A., Reines, A. E., Johnson, K. E., & Walker, L. M. 2014, AJ, 147, 43
Kewley, L. J., & Dopita, M. A. 2002, ApJS, 142, 35
Kobulnicky, H. A., & Johnson, K. E. 1999, ApJ, 527, 154
Kroupa, P. 2001, MNRAS, 322, 231
Kruijssen, J. M. D., Schruba, A., Chevance, M., et al. 2019, Natur, 569, 519
Krumholz, M. R., McKee, C. F., & Bland, -H., Jr. 2019, ARA&A, 57, 227
Lada, C. J., & Lada, E. A. 2003, ARA&A, 41, 57
Leitherer, C., Schaerer, D., Goldader, J. D., et al. 1999, ApJS, 123, 3
Lin, Z., Calzetti, D., Kong, X., et al. 2020, ApJ, 896, 16
Matthews, A. M., Johnson, K. E., Whitmore, B. C., et al. 2018, ApJ, 862, 147
Messa, M., Adamo, A., Calzetti, D., et al. 2018a, MNRAS, 477, 1683
Messa, M., Adamo, A., Östlin, G., et al. 2018b, MNRAS, 473, 996
Messa, M., Adamo, A., Östlin, G., et al. 2019, MNRAS, 487, 4238
Peters, W. L., Freeman, K. C., Forster, J. R., Manchester, R. N., & Ables, J. G. 1994, MNRAS, 269, 1025
Pfalzner, S., & Kaczmarek, T. 2013, A&A, 559, A38
Reines, A. E., Nidever, D. L., Whelan, D. G., & Johnson, K. E. 2010, ApJ, 708, 26
Ryon, J. E., Bastian, N., Adamo, A., et al. 2015, MNRAS, 452, 525
Ryon, J. E., Gallagher, J. S., Smith, L. J., et al. 2017, ApJ, 841, 92
Silva-Villa, E., & Larsen, S. S. 2012, MNRAS, 423, 213
Sukhbold, T., Ertl, T., Woosley, S. E., Brown, J. M., & Janka, H. T. 2016, ApJ, 821, 38
Tsai, C.-W., Turner, J. L., Beck, S. C., Meier, D. S., & Ho, P. T. P. 2009, AJ, 137, 4655
Turner, J. L., & Beck, S. C. 2004, ApJL, 602, L85
Vacca, W. D., Johnson, K. E., & Conti, P. S. 2002, AJ, 123, 772
Vázquez, G. A., & Leitherer, C. 2005, ApJ, 621, 695
Whelan, D. G., Johnson, K. E., Whitney, B. A., Indebetouw, R., & Wood, K. 2011, ApJ, 729, 111
Whitmore, B. C., Brogan, C., Chandar, R., et al. 2014, ApJ, 795, 156
Whitmore, B. C., Chandar, R., Kim, H., et al. 2011, ApJ, 729, 78
Whitmore, B. C., Chandar, R., Lee, J., et al. 2020, ApJ, 889, 154
Zackrisson, E., Bergvall, N., Olofsson, K., & Siebert, A. 2001, A&A, 375, 814
Zackrisson, E., Rydberg, C.-E., Schaerer, D., Östlin, G., & Tuli, M. 2011, ApJ, 740, 13